Title
Laboratory Experimental and Numerical Investigations of Heat Extraction From Porous Media by Means of CO2

Author
Magliocco, Mario Joseph

Publication Date
2015

Peer reviewed|Thesis/dissertation

Laboratory Experimental and Numerical Investigations of Heat Extraction From Porous Media by Means of CO2

by

Mario Joseph Magliocco

A dissertation submitted in partial satisfaction of the

requirements for the degree of

Doctor of Philosophy

in

Engineering - Civil and Environmental Engineering

in the

Graduate Division

of the

University of California, Berkeley

Committee in charge:

Professor Steven D. Glaser, Chair
Assistant Professor Scott J. Moura
Assistant Professor Duncan S. Callaway

Spring 2015

Laboratory Experimental and Numerical Investigations of Heat Extraction From Porous Media by Means of CO2

Abstract

Laboratory Experimental and Numerical Investigations of Heat Extraction From Porous Media by Means of CO2

by

Mario Joseph Magliocco

Doctor of Philosophy in Engineering - Civil and Environmental Engineering

University of California, Berkeley

Professor Steven D. Glaser, Chair

The use of CO_2 as a heat transfer fluid has been proposed as an alternative to water in enhanced geothermal systems (EGS) and in CO_2-plume geothermal systems (CPG). Numerical simulations have shown that under expected EGS operating conditions, CO_2 would achieve more efficient heat extraction performance compared to water, especially at sites with low geothermal temperatures and low subsurface heat flow rates. With increased interest in carbon capture and sequestration (CCS), the possibility of combining geothermal energy production with carbon sequestration is actively being explored. Simulations have shown that CO_2-based geothermal energy production could substantially offset the cost of CCS. Since numerical models are critical for the planning and operation of geothermal systems that employ CO_2 as the working fluid, it is important to validate the results of the current numerical tools against real-world experimental data.

A laboratory apparatus was assembled that is capable of operating at temperatures up to 200 °C, pressures up to 34.5 MPa, and flow rates up to 400 mL/min. The experimental system was designed such that measurements and controls at the boundaries could be readily modeled. It was found that the dynamic physical behavior and chemical properties of CO_2 create problems with sealing, flow control, and safety. The unique challenges of handling, control, and measurement of supercritical CO_2 are addressed in this work as well as tools, techniques and materials identified for overcoming them. The described flow system could be applied to the selective extraction of components from organic materials, as well as the extraction of heat from porous media.

Using the assembled apparatus, heat transfer behavior of flowing dry supercritical CO_2 through a heated porous medium was investigated and experimental results were compared with a numerical model using TOUGH2 with the ECO2N module. In addition, experiments were performed using (1) CO_2 and (2) water as the working fluids under similar operating conditions in order to compare the heat transfer behavior and the overall heat extraction rates. We have made estimates of the density and the effective thermal conductivity of our saturated porous media, and have found that both properties change significantly during the

course of experiments. The large changes in CO_2 density, due to decreasing system temperatures, can result in fluid accumulation in the system that may have significant impacts on geothermal reservoir management. The large changes in thermal conductivity as a function of pressure and temperature are of concern because the standard TOUGH2 code does not update the thermal conductivity of the system during the course of a simulation.

A detailed TOUGH2 model of the experimental system was created and was calibrated against the experimental data. The calibration results of optional thermal conductivity updating code included with the new ECO2N v2.0 module was compared against calibration using the standard constant effective thermal conductivity assumption. It was found that including effective thermal conductivity updating in the model resulted in an simpler calibration process that produced less missfit across all experiments than when a single estimated thermal conductivity value was used.

To the loving memory of Karen and Melvin Magliocco who made this all possible, and to Mai who makes it all worthwhile.

Contents

List of Figures

List of Tables

Acknowledgments

My father Melvin never lived to see me attend the university where he earned a living for his young family, but it is because of his being that I ended up there. The unfailing kindness and love of my mother Karen gave me the strength and stability needed to make it through the years of hard work. They never doubted me and I miss them both dearly.

I would like to thank my advisor Steve Glaser who gave me the support and freedom to explore while having my back when things got rough. I would also like to thank Tim Kneafsey who gave me unfettered access to his equipment and experience.

I would also like to thank my lab mates Greg Mclaskey, Chris Sherman, Ziran Zhang, and Paul Selvadurai who provided support and camaraderie in life and academics. To my friends and fellow students Nate Butler, and Augustus Smarkel who helped me through the battlefield that is UC Berkeley undergraduate studies, thank you.

Many thanks to my siblings, Dennis, David, and Karmela for providing an anchor for my world.

Finally, I would like to thank my lovely and amazing wife and friend Mai, who I can't help falling in love with on a regular basis. She made it all work, she made it all make sense.

Chapter 1

Initial Experimental and Numerical Studies of CO_2 Heat Extraction

1.1 Introduction

Geothermal energy is a vast resource that, if efficiently utilized, could contribute significantly towards meeting the base load energy demand in the United States (Tester et al. 2006). Traditional commercial geothermal electricity production is dependent on a number of factors including an optimized combination of geological conditions such as presence of hydrothermal fluid, high heat flux, high rock permeability and/or high rock porosity. Enhanced (or Engineered) Geothermal systems (EGS) are an attempt to exploit geothermal energy in locations where these conditions are not optimal (Tester et al. 2006). Most EGS strategies involve reservoir stimulation to overcome the lack of porosity and/or permeability of the rock using various chemical and physical processes, as well as supplying the needed heat transfer process fluid (e.g. water or CO_2) (Majer et al. 2007). The novel concept of using supercritical CO_2 as the working fluid in EGS for both reservoir creation and heat extraction was first proposed by Brown (Brown 2000). Subsequent work includes numerical simulations of a five-spot well pattern in a hot dry rock (HDR) system, which estimated an approximately 50% greater heat extraction rate using CO_2 instead of water given the same operating conditions (Pruess 2006). The advantages of using CO_2 over water as the process fluid in a closed loop HDR system include (1) much lower viscosity of CO_2 means that substantially larger mass flow rates can be achieved for a given pressure drop between injection and production points; and (2) much larger density difference between cold fluid in the injection well and hot fluid in the producer results in increased buoyancy forces for CO_2, which could reduce or even eliminate pumping requirements. As an ancillary benefit, practical operation of a CO_2-based system would result in de facto carbon sequestration due to the amount of CO_2 required and fluid loss to the surrounding formations (Brown 2000; Pruess 2006). Currently the large-scale use of CO_2 for EGS energy production is impractical due to the cost of capturing, pressurizing, and transporting CO_2 (Eastman, Muir, and Energy

2013), as well as concerns of induced seismicity from the injections (Majer et al. 2007). If environmentally driven public policy changes require the capture and sequestration of CO_2 on a significant scale, it could be possible to produce geothermal energy at the sequestration site to generate electricity or to simply offset the costs of sequestration (Randolph and Saar 2011). To avoid concerns of induced seismicity due to hydraulic fracturing a new concept was developed in which CO_2 is used as a working fluid in geologic reservoirs with high porosity, high permeability, and an overlying low-permeability cap rock (Randolph and Saar 2011). This strategy has been named CO_2-plume geothermal (CPG) in order to differentiate it from conventional EGS systems that may make use of a fracturing stage of reservoir development. In light of the promising modeling results and continued interest in CO_2-based geothermal energy production, it is necessary to validate the theoretical tools with practical laboratory and field experiments. This paper presents the design, implementation, and results of a laboratory-scale CO_2-based heat extraction experiment with the goals of producing a data set that can be compared to results of reservoir numerical modeling tools at the tested conditions, exploring the heat transfer behavior of the system under various operating conditions, and comparing the performance of CO_2 and water based systems operated under the same conditions. TOUGH2/ECO2N (Pruess 2004; Pruess and Spycher 2007) was the modeling tool selected because the ECO2N module has incorporated CO_2 properties up to temperatures of 110 °C and pressures up to 60 MPa.

1.2 Experiment Description

This project consisted of two major efforts: the creation of laboratory-derived data sets of heat transfer in geologic media using supercritical CO_2, and the creation of a well-behaved numerical model of the physical experiment evaluated using TOUGH2 and ECO2N. For these experiments, temperature-controlled CO_2 was injected under specified conditions into a large heated, sand-filled pressure vessel, and measured temperatures at 23 locations within the sample. Other measurements included the mass rate of fluid injection, injection pressure, vessel outlet pressure, and the pressure difference between the injection and outlet ports of the vessel.

Experimental Apparatus

The apparatus consists of a temperature-controlled pressure vessel filled with a porous medium through which temperature-controlled fluid could be introduced by means of high-pressure, high-flow rate pumps (Figure 1.1). The pumps could be operated to provide a constant fluid-injection rate, or a constant differential pressure. The fluid was delivered by a pair of Quizix C-6000-5K pumps, capable of 34.5 MPa and 400 mL/min fluid delivery rate. The pumps can precisely control continuous and pulse-free flow with a resolution of 27.2 nL. To ensure that the pumps were filled with high-density liquid CO_2, the injection fluid was passed through a chiller before entering the pumps. The temperature of the fluid leaving the

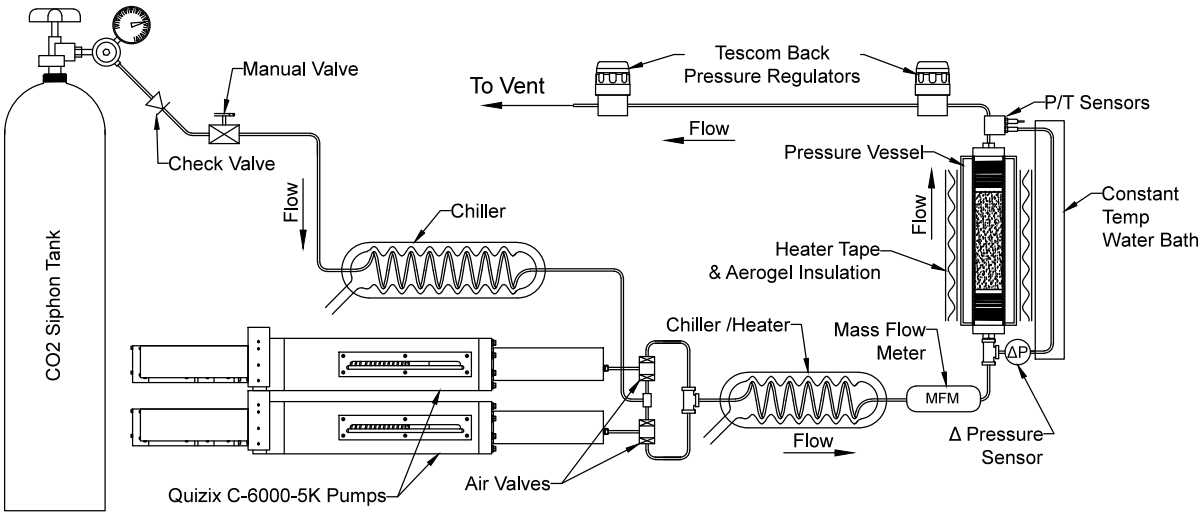

Figure 1.1: Diagram of experimental apparatus. Fluid was supplied by a siphon style CO_2 tank. Fluid was driven by a pair of pumps and fed through air-actuated valves. The fluid was then either chilled or heated before it passed through a mass flow meter and into the bottom inlet of the cylindrical pressure vessel that was oriented vertically. A differential pressure sensor was connected hydraulically to the inlet and outlet of the vessel via a temperature-controlled length of tubing that was also oriented vertically. Pressure and temperature sensors were located at the outlet (top) of the vessel. Pressure in the fluid exiting the vessel was reduced by a pair of feedback controlled back pressure regulators, which released the fluid to the atmosphere. The vessel was packed with sand and wrapped in heater tape, which was subsequently covered by a fitted aerogel insulation blanket.

pumps was chilled or heated depending on the desired experimental parameters. To quantify the mass of CO_2 entering the sample, the injection fluid passes through a Siemens Sitrans MASS 2100-D3 coriolis-style mass flow meter before entering the vessel.

The pressure vessel (High Pressure Equipment Company TOC 31-20) was a hollow type 304 stainless steel cylinder with an inside diameter of 9.1 cm, outside diameter of 12.7 cm, 50.8 cm distance between the type 316 stainless steel end caps secured by 4340 alloy steel caps. The vessel has a pressure safety rating of 34.5 MPa. Instrumentation and flow access to the interior of the vessel is through three axial passages through one end cap (typically the bottom end cap), and one passage through the other (top). The central passages through the end caps were used as the injection and production ports and the remaining two passages were used exclusively to pass thermocouples through. The vessel was oriented vertically since it has been shown that even for small length scales, buoyant effects of CO_2 can have a large effect on the dynamics of a CO_2-based system (Liao and Zhao 2002). For a horizontal flow arrangement, buoyant forces can result in pressure gradients that are oriented perpendicular to the vessel axis, complicating the dynamics and test evaluation. For modeling and comparison purposes, the experiments were operated vertically such that the flow path was in

the same orientation as the gravity-induced pressure gradient. Temperature measurements within the sample were made with 23 stainless-steel clad type-T thermocouples, which have a small diameter (0.79 mm) in order to increase the sensor response time and to minimize disturbance to fluid flow. The thermocouples were arranged at various elevations and radii in the sample such that each successive vertical level was offset angularly to minimize vertical sensor shadowing (Figure 1.2, Table 1.1). The offset angle used was based on the "Golden Angle" (137.5°), found in plant phyllotaxis that has been shown to minimize shadowing (King, Beck, and Lüttge 2004). At one elevation in the porous media, two thermocouples were mirrored so that they were both at the same radial distance from the central axis of the vessel to test the assumption of a radial symmetry in the heat transfer process. An Agilent digital multimeter connected to a computer recorded the thermocouples voltages and converted them to temperature.

Because the end caps are massive and heated, the $\frac{1}{4}$-inch inner diameter injection port of the vessel was lined with a length of $\frac{1}{4}$-inch outer diameter nylon tubing through the end cap in order to provide thermal insulation for the injected fluid as it passed through the end cap. The injection port was also fitted with a single thermocouple, mounted where the injected fluid enters the sample space to measure the temperature of the CO_2 as it entered.

The sand used in the test sample was prepared from F95 Ottawa silica sand (U.S. Silica). Sieving and washing resulted in a narrow grain size distribution (Figure 1.3). The mean grain size falls between 105 and 147 microns with no measurable portion below a grain size of 45 microns. The sand was dry-placed in the vessel in multiple lifts with vibratory compaction between lifts. This method produced a relative density of 84 percent. The porous sample properties are listed in Table 1.2. Quartz crystal is highly anisotropic and the thermal conductivity can vary greatly depending on the direction of the crystal axis (Powell, Ho, and Liley 1966). The value used for the solid sand grains is based on a random distribution of crystal axis orientations using the arithmetic mean as calculated by Woodside (Woodside and Messmer 1961).

The vessel was wrapped with five eight-foot lengths of fiberglass fabric covered heat tape that extended around the exterior of the cylinder and both end caps, with an output of 1248 W each for a total possible output of 6240 W. The heat tape thermal output was regulated by a closed loop-controller that used the feedback from a single thermocouple secured on the vessel exterior to approximate a constant temperature boundary based on a set point. Finally the vessel was wrapped in an aerogel insulation jacket and sealed. The aerogel insulation jacket was constructed with a 5 mm thick internal layer of silica aerogel 20-23 W/(m K) reinforced with a non-woven, glass-fiber batting, which was then covered with a reflective Teflon material.

The pressure at the outlet of the vessel was controlled by a pair of digital back pressure regulators arranged in series. The fluid exiting the back pressure regulators was vented to the atmosphere. A differential pressure sensor was located at the base of the vessel and hydraulically connected to the inlet and outlet of the vessel by means of $\frac{1}{8}$-inch stainless steel tubing. The vertically oriented length of tubing that connected the differential pressure sensor to the inlet was encased in a constant-temperature water bath. It was found in

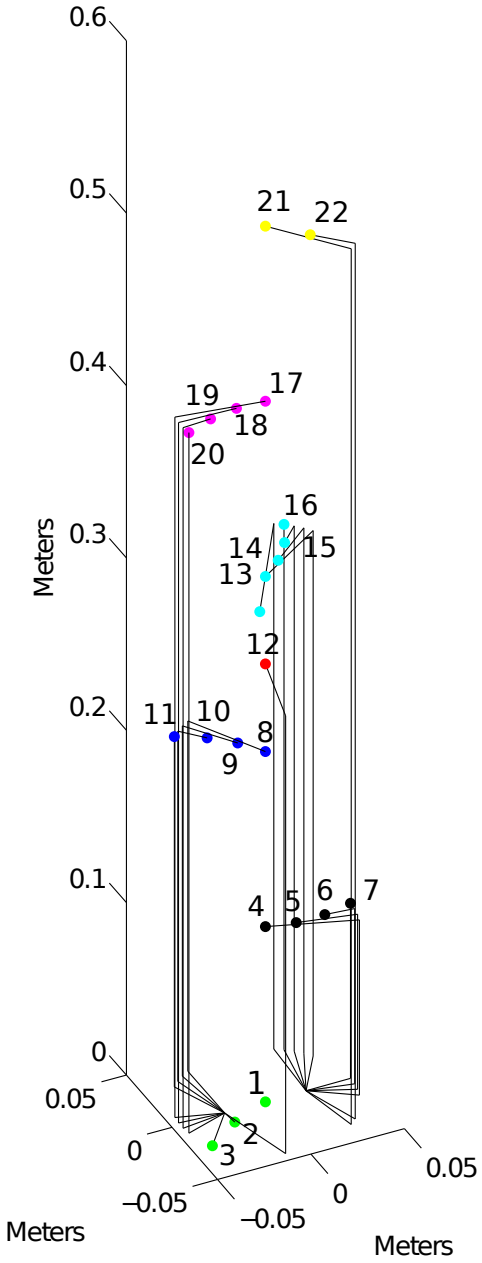

Figure 1.2: Orthographic diagram of thermocouple placement inside the vessel. Axis units are in meters.

Thermocouple	Elevation (cm)	Radii (cm)
1	0	0
2	0	2.3
3	0	4.6
4	10.2	0
5	10.2	1.5
6	10.2	3.0
7	10.2	4.6
8	20.3	0
9	20.3	1.5
10	20.3	3.0
11	20.3	4.6
12	25.4	0
13	30.5	0
14	30.5	1.5
15	30.5	3.0
16	30.5	4.6
17	40.6	0
18	40.6	1.5
19	40.6	3.0
20	40.6	4.6
21	50.8	0
22	50.8	2.3

Table 1.1: Location and numbering of thermocouples. This table excludes the thermocouple that duplicates the radial position of number 15.

early tests, before the connecting tubing was encased in a bath, that the small variations in fluid temperature in this section of tubing resulted in large variations in fluid density that significantly impacted the differential pressure reading. The constant temperature bath was then added to impose a temperature on the fluid that hydraulically connects the outlet of the vessel with the differential pressure transducer that was located below at the inlet of the vessel. This temperature was measured throughout the experiment but was kept at a nominal temperature of 10 °C by means of a laboratory water chiller/circulator. Since the outlet pressure was specified and controlled by back pressure regulators, and was held constant throughout the experimental runs (within a few thousand Pascals except at flow initiation), and the water bath temperature was held constant (within a few degrees of 10 °C), the weight of the fluid in the connecting tubing was also relatively constant and therefore did

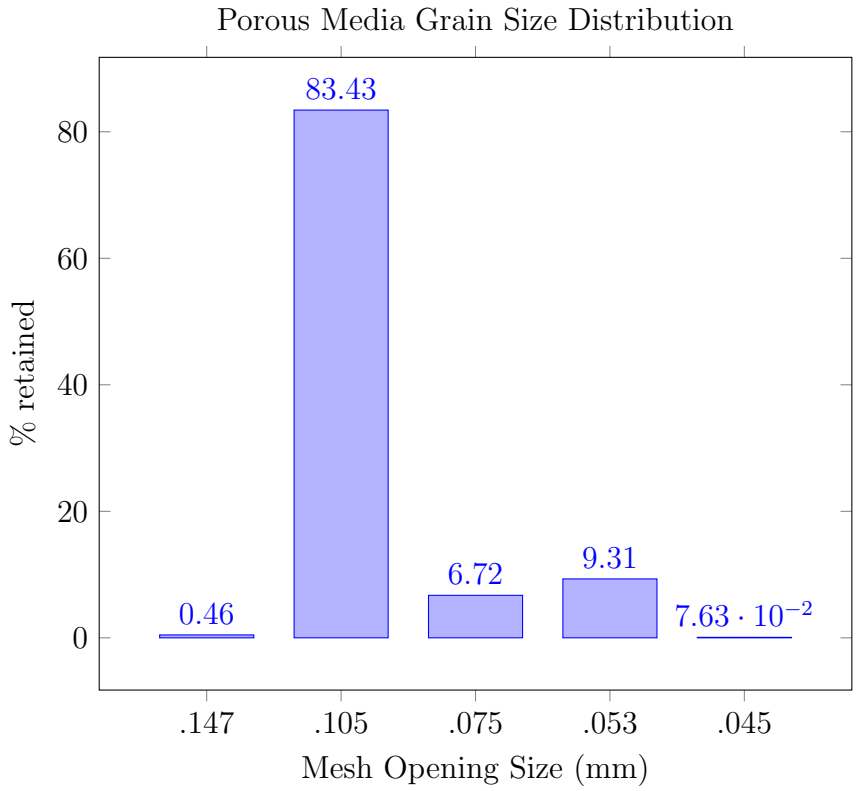

Figure 1.3: Grain size distribution of sorted Ottawa sand.

not significantly affect the differential pressure reading. The outlet pressure and the water bath temperature were measured during the experiment so that any variations were recorded and could be used to calculate any changes in the density of the fluid in the tubing, then be used to correct the differential pressure reading if needed. The short section of tubing that hydraulically connected the differential pressure sensor to the inlet was not incased in a water bath since it was oriented horizontally. The constant temperature bath around the differential pressure connection tubing would not be necessary when water was employed as a working fluid as water does not significantly change density with changes in pressure and temperature at the scale of the experiment.

Software was developed that incorporates experimental control and data acquisition. All sensor readings were collected by a single Labview-based program that allows for accurate time synchronization of experimental data. The program was capable of controlling the pumps and the back pressure regulators. Combining these functions allowed for a tightly integrated experimental setup, faster data processing, faster experimental turnaround time, and reduced experimental errors.

Porous Core Properties	
Total Core Length	$L = 50.8\,cm$
Cross Sectional Area	$A = 6.54 \times 10^{-3}\,m^2$
Crystalline Quartz Density	$\rho_R = 2650\,kg/m^3$
Crystalline Quartz Specific heat	$C_R = 830\,J/(kg\,K)$
Crystalline Quartz Thermal Conductivity	$8\,W/(m\,K)$
CO_2 Saturated Sand Effective Thermal Conductivity Range	0.22-1.0 $W/(m\,K)$
Permeability	$k = 9.3 \times 10^{-13}\,m^2$
Porosity	$\phi = 41\%$
Mean Grain Size d_{50}	d_{50} 0.105 mm

Table 1.2: Design case system properties.

Experiment Procedure

At the experiment initiation the sand-packed vessel was filled with CO_2 and pressurized to the experiment pressure, and the vessel was heated to the desired initial temperature. The pumps and tubing were then filled with CO_2 and pressurized to the vessel pressure. The back pressure regulators were set to the desired outlet pressure, the heater tape was turned off, and CO_2 at the specified temperature and pressure was injected into the bottom of the vessel at a prescribed volumetric flow rate. The pumps were operated in an alternating order, while one pump was injecting fluid into the sample, the other pump would refill. Multiple pump volumes were used in the experiments, which were terminated as the system approached equilibrium. The temperature of the injected fluid was controlled by the laboratory water chiller-circulator that pumped water through the pump water jackets and the water bath heat exchanger located before the vessel inlet. The laboratory water chiller was set for a nominal temperature of 10 °C. The actual injection temperature was measured by a thermocouple located at the inlet of the sample. All thermocouple readings were collected at a frequency of 10 samples per minute.

Modeling

A 2D axisymmetric model of the sample and experimental apparatus was implemented in TOUGH2/ECO2N (Pruess 2004; Pruess 2007), and included the porous medium, steel vessel, and inlet and outlet material domains. The majority of the modeling work was executed on a dual core 64-bit x86 processor running Apple OSX operating system. A suite of Matlab scripts was written to allow automatic generation of the mesh file, input files, and extraction and plotting of the simulation data. A mesh generation script allowed properly sized models

to be produced rapidly with user selectable quantity of cells in each domain axis. For the modeling results shown in this paper a resolution of 44 layers in the vertical direction and seven annuli in the radial direction were used with the same dimensions as the actual experimental apparatus. A cell was set as a mass flow rate source for the injection point of the model. The outlet of the vessel was modeled as a time-independent Dirichlet boundary by use of an "inactive" cell (Pruess 2004). The exterior of the vessel, excluding the inlet and outlet, was treated as a no-flux boundary by omitting any flow connections across the surface. The initial conditions such as the initial temperature distribution were generated by a Matlab script that analyzed the data from the experimental run being modeled.

1.3 Results and Discussion

Experimental Results

Sixteen single-phase CO_2 experiments were performed under a variety of conditions using slightly different versions of the experimental apparatus. An experiment was also performed with single-phase water, and an experiment in which CO_2 was injected into a water-saturated core. Here data is presented for three representative single-phase CO_2 experiments operated under three different parameters listed in Table 1.3. The temperature data from the twenty-two (ignoring the redundant thermocouple) thermocouples from a typical experimental run is shown in Figure 1.4. The thermocouples are numbered primarily in order of increasing radii and secondarily by increasing elevation in the vessel. Thermocouple 1 for example is located on the central axis at the bottom of the vessel, while thermocouple number 22 is located near the vessel wall at the top of the vessel (Figure 1.2). All temperature history plots in this paper use the same color and line style scheme to indicate the thermocouple location. The plot color indicates the thermocouple elevation (corresponding to colored markers in Figure 1.2), and the line style indicates the radial location, going from a solid line at the central axis, followed by dot-dashed, dashed, and finally a dotted line indicating a location at the vessel wall.

Test #	Initial Average Vessel Temperature (C)	Back Pressure (MPa)	Flow Rate (mL/min)	Estimated Mean Initial Pe	Estimated Mean Final Pe	Estimated Mass Accumulation (g)
1	86	13.8	100	2.8×10^3	1.1×10^3	652
2	52	8.3	200	1.1×10^4	2.0×10^3	872
3	59	8.3	100	1.2×10^4	1.2×10^3	816

Table 1.3: Test Conditions

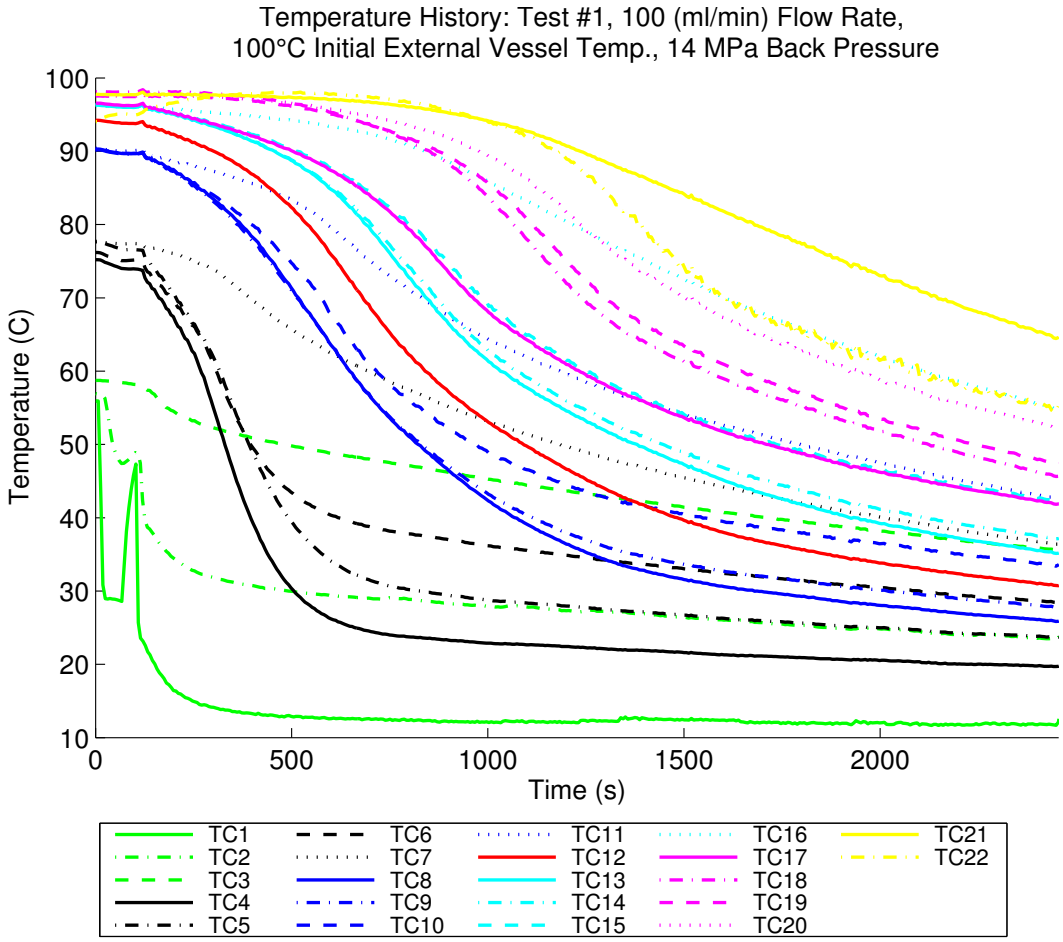

Figure 1.4: Temperature vs time data from twenty-two thermocouples from Experiment 1.

In all experiments, there was an initial vertically oriented temperature gradient present in the saturated medium with a lower temperature at the base of the vessel. Upon introduction of the cold CO_2 at the sample bottom a temperature front developed. The temperature front can be seen as a downward trend in Figure 4 as it passes axially through the sample past the measurement locations. The initial sharp temperature drop that begins at time t = 0 in the plot for Thermocouple 1 at the injection port (green solid curve), occurred at the same time that the pump outlet valve was opened before injection was initiated and likely resulted in a small amount of cold injection fluid entering the vessel. The subsequent spike in temperature (approximately 17 °C) seen at the inlet (solid green line) is likely due to the passage of a hot slug of CO_2 that became heated as it rested in the tubing that passed through the end cap before injection began and after the pump valves were opened. There was also a very small transient increase in temperature (approximately 0.3 °C) at the other thermocouple elevations (TCs 4-22) after the start of injection that is a response to brief increase of pressure in the vessel (approximately 0.48 MPa) due to a small delay in the operation of the back

pressure regulator transitioning from the no-flow state.

The temperature fronts as exhibited by the temperature history plot from Experiment 1 (Figure 1.4) had a relatively smooth shape and gentle slope when compared with the other experiments that were operated with a higher CO_2 injection rate (discussed below). After injection was initiated, a radial temperature gradient developed, indicated by curves from thermocouples at the same elevation (same color) that began at the same initial temperature and diverged over time. This behavior can be easily seen in the way the blue set of curves (20 cm elevation in the sand pack) diverge in temperature after they were all initially at 90 °C. As the experiment progressed, the more exterior locations (dotted lines) generally trend towards a higher temperature than those more centrally located (solid lines), because of the heat stored in the wall of the steel vessel. This behavior is not seen at the top of the vessel (yellow lines), most likely due to the geometry at the outlet end of the vessel. The initial temperature distribution and developing radial temperature gradients are more apparent in the contour plots of the temperature data. Figure 1.5 shows the interpolated temperatures for a vertical cross section of the vessel at different times in Experiment 1.

Thermal Transport

The characteristic rates of the advective and conductive processes can be compared using the dimensionless Peclet number (Pe). The Peclet number can be expressed as the ratio of the time required for both processes to pass across the length scale in question, or conduction time over advection time.

$$Pe = \frac{t_{cond}}{t_{adv}} = \frac{\frac{L^2}{D_{th}}}{t_{ad}} = \frac{L^2}{D_{th}(\frac{L}{V_p})} = \frac{LV_p}{D_{th}} \tag{1.1}$$

In Equation 1.1 t_{cond} is the characteristic thermal conduction time, t_{ad} is the characteristic fluid advection time, D_{th} is the thermal diffusivity, L is the characteristic length, and V_p is the pore velocity. This formulation ignores the thermal retardation factor effect on thermal advection and instead compares the bulk stagnant thermal conduction time to the fluid mass advection time. This assumes a null specific heat capacity of the sand for the advection. The bulk pore velocity for the experiment was oriented in the vertical direction as the fluid was pumped into the inlet at the bottom of the vessel and was produced at the outlet at the top of the vessel. Since the flow in the vessel was oriented vertically, all the Peclet numbers calculated and referenced in this paper were for the vertical direction. Heat transfer in the radial direction from the heated stainless steel vessel walls toward the center of the sample was largely conductive/dispersive due to the lack of imposed flow in the radial direction. The bulk stagnant thermal conduction time was found by estimating the thermal diffusivity of the sand and CO_2 at experimental conditions

$$D_{th} = \frac{\lambda_{eff}}{\rho_{avg} C_{p,avg}} \tag{1.2}$$

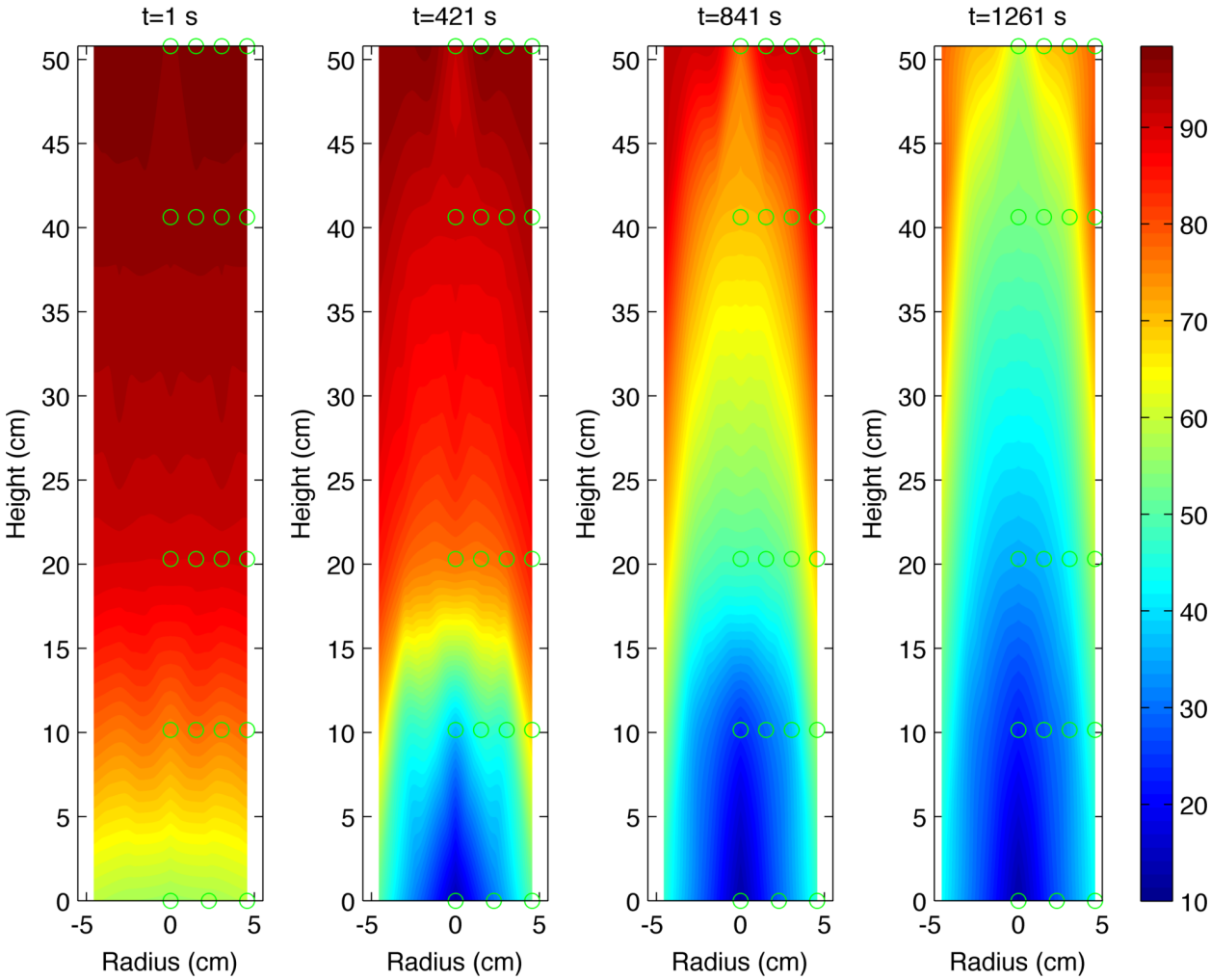

Figure 1.5: Interpolated contour plots of the internal temperatures of Experiment 1 at times t=1s, 421s, 841s, and 1,261 seconds. The CO_2 inlet temperature is shown in Figure 1.4. A 2D spline interpolation was used, and the relatively sparse data set resulted in some artifacts, for this reason the data from the single thermocouple at the elevation of 30 cm (TC 12) was omitted. Thermocouple locations are indicated by small circles.

where λ_{eff} is the estimated effective thermal conductivity of the CO_2-sand matrix, ρ_{avg} is the volumetric average density of the CO_2 sand matrix, and $C_{p,avg}$ is the average of the specific heat of the CO_2-sand matrix. An equation from Kunii and Smith (Kunii and Smith 1960) that assumes spherical particles in a packed bed, and neglects radiation and heat conduction through the grain contacts, was used to estimate the effective thermal conductivity of the CO_2-sand matrix. This equation was found to match well with experimental measurements even at solid to fluid thermal conductivity ratios over 20 (Woodside and Messmer 1961), without the need for finding extensive properties such as grain contact pressure and area.

The estimated effective thermal conductivity of the CO_2-sand matrix, λ_{eff} is

$$\lambda_{eff} = \lambda_f \left[\phi + \frac{1-\phi}{\epsilon + \frac{2}{3}\lambda_f/\lambda_s} \right] \tag{1.3}$$

where λ_f is the thermal conductivity of the fluid, λ_s is the thermal conductivity of the solid, ϕ is the porosity, and ϵ is a parameter based on the packing configuration of spherical particles. The parameter ϵ is found by linearly interpolating between ϵ_1 which corresponds to a loose packing of spheres ($\phi = 0.476$) and ϵ_2 which corresponds to a close packing of spheres ($\phi = 0.260$) by means of the equation:

$$\epsilon = \epsilon_2 + \frac{(\phi - 0.260)(\epsilon_1 - \epsilon_2)}{0.217} \tag{1.4}$$

Kunii and Smith (Kunii and Smith 1960) provide a plot that relates the values of ϵ_1 and ϵ_2 to the ratio of solid to fluid thermal conductivities (λ_s/λ_f). The thermal conductivity and all other CO_2 properties used for the calculations outside of TOUGH2 were based upon data from the NIST Standard Reference Database 69 (Lemmon, McLinden, and Friend 2005).

Because conditions in the experiment changed over time, the CO_2 density changed as internal vessel temperatures changed, it was impossible to calculate a single Pe number that was valid for all times and all locations inside the vessel. A Pe number was calculated for the initial and final bulk conditions of the experiments neglecting CO_2 accumulation, which would alter the pore velocity throughout the column. The estimated initial and final Peclet numbers are shown in Table 1.3.

The interplay between advective and conductive transport is also demonstrated by the shape of the temperature vs time curves. An almost purely advective dominated process would feature sharp thermal fronts, a near vertical slope at the time when the cold fluid slug reached the thermocouple, and would have a higher Pe number. A conductive dominated process would exhibit a gentle slope with smooth transitions, and would correspond to a lower Pe number. For Experiment 1 (Figures 1.4 and 1.5 above) the estimated Pe number for the initial condition was 2.8×10^3 and the estimated Pe number for the final condition was 1.1×10^3. Experiment 2 (Figure 1.6 and 1.7) which was operated at twice the flow rate of Experiment 1, exhibits a much more steeply sloped temperature front that, along with the higher estimated Pe numbers (1.1×10^4 initial - 2.8×10^3 final), indicates that the heat transfer process was advectively dominated.

CO_2 Accumulation

Two methods were used to measure the mass flow rate at the inlet of the vessel: the lookup method and the mass flow rate meter. The look-up method used the volumetric flow rate of the pump, the temperature and pressure of the fluid exiting the pumps, and a density lookup table for CO_2 (Lemmon, McLinden, and Friend 2005) in order to estimate the mass flow rate delivered. The look up method for determining mass flow delivered to the vessel

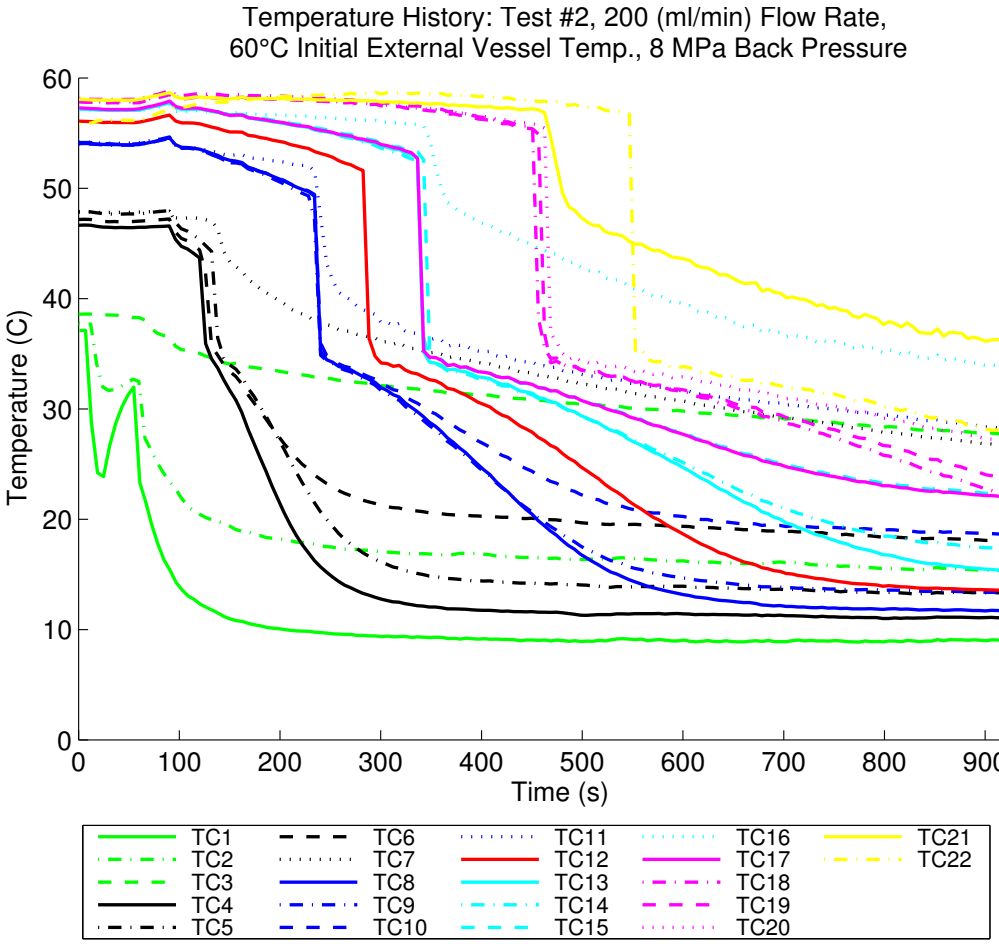

Figure 1.6: Temperature vs time data from twenty-two thermocouples from Experiment 2.

from the pump corresponded well with the data from the mass flow meter at the injection side of the vessel. CO_2 accumulation was found to be significant as the temperature of the fluid in the vessel decreased. In Experiment 1 the mean initial vessel temperature of 87 °C and initial pressure of 13.8 MPa corresponds to a CO_2 density of 341 kg/m^3; at the end of the experimental run (t=2350s), the mean vessel temperature was 33 °C which at 13.8 MPa corresponds to a CO_2 density of 814 kg/m^3. This change of temperature results in an approximate density increase of 2.4 times, or an accumulation of 652 g of CO_2 in the pore space. The estimated accumulation of CO_2 in the vessel for all of the experiments can be found in Table 1.3.

CO_2 vs Water

To compare the performance of CO_2 heat extraction with that of water, a single-phase water run at the same temperature and pressure as a CO_2 run was performed (Figure 1.9).

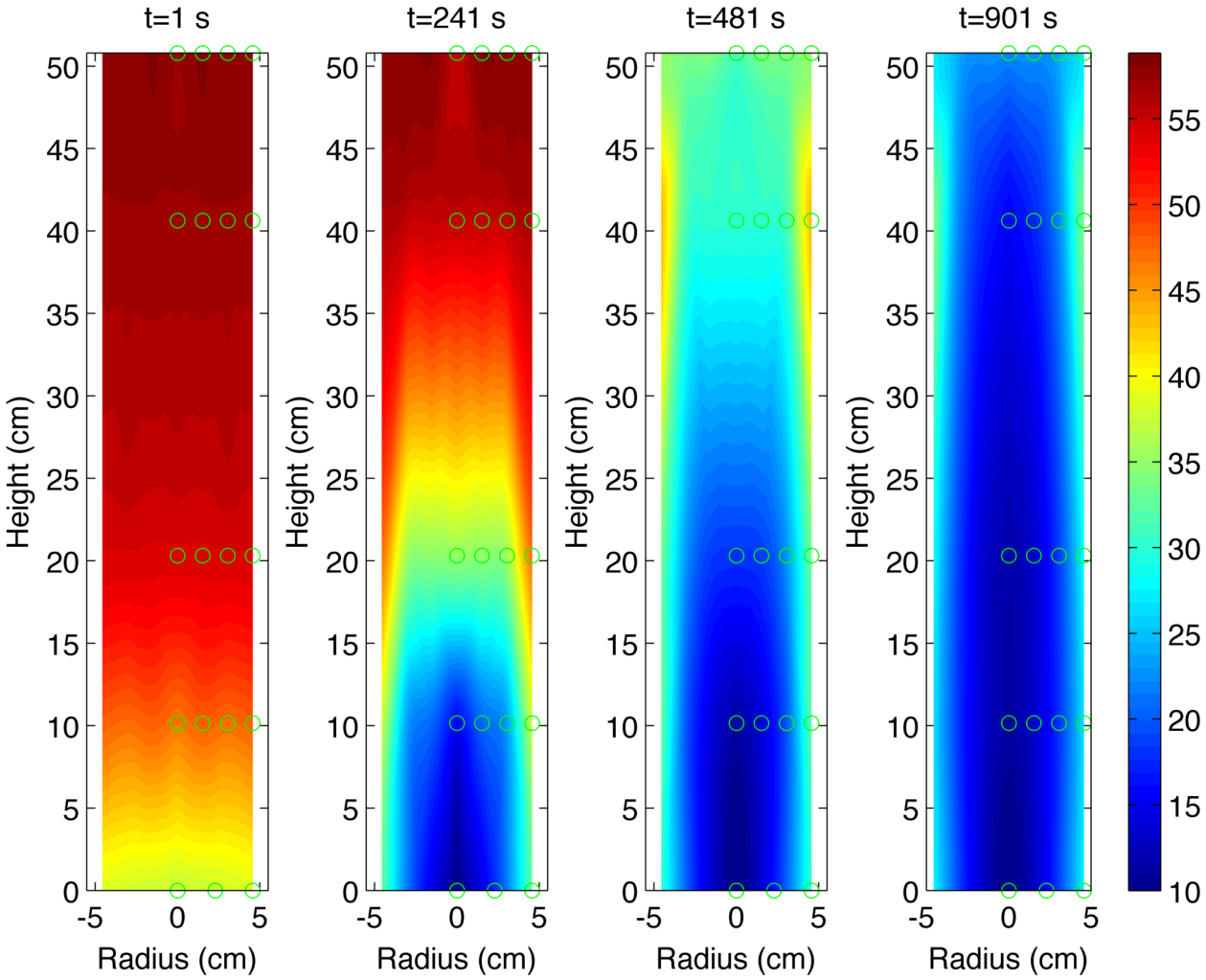

Figure 1.7: Interpolated contour plots of the internal temperatures of Experiment 2 at times t=1s, 241, 481, and 901 seconds. Thermocouple locations are indicated by small circles.

Both experiments were performed with an older, less refined version of the apparatus that contained a less dense thermocouple array. To compare the two working fluids, a volumetric fluid injection rate of 150 mL/min, an initial sample temperature of 75 °C, and a back pressure of approximately 10 MPa were selected. The CO_2 and water experiments had approximately the same pressure differential across the sample for both water and CO_2 (0.2 MPa), and a similar mass flow rate (2.51 g/s for water, and a range of 2.3 to 2.04 g/s for CO_2), which allowed a more straightforward comparison of the performance of the two fluids. The injected water and CO_2 increased in temperature after the first two pump volumes because in these earlier tests the injection fluid was recycled. The CO_2 plot shows a much steeper temperature front indicating a more advection-dominated flow than the water experiment. This is due to the lower CO_2 fluid thermal conductivity than water under the experimental conditions.

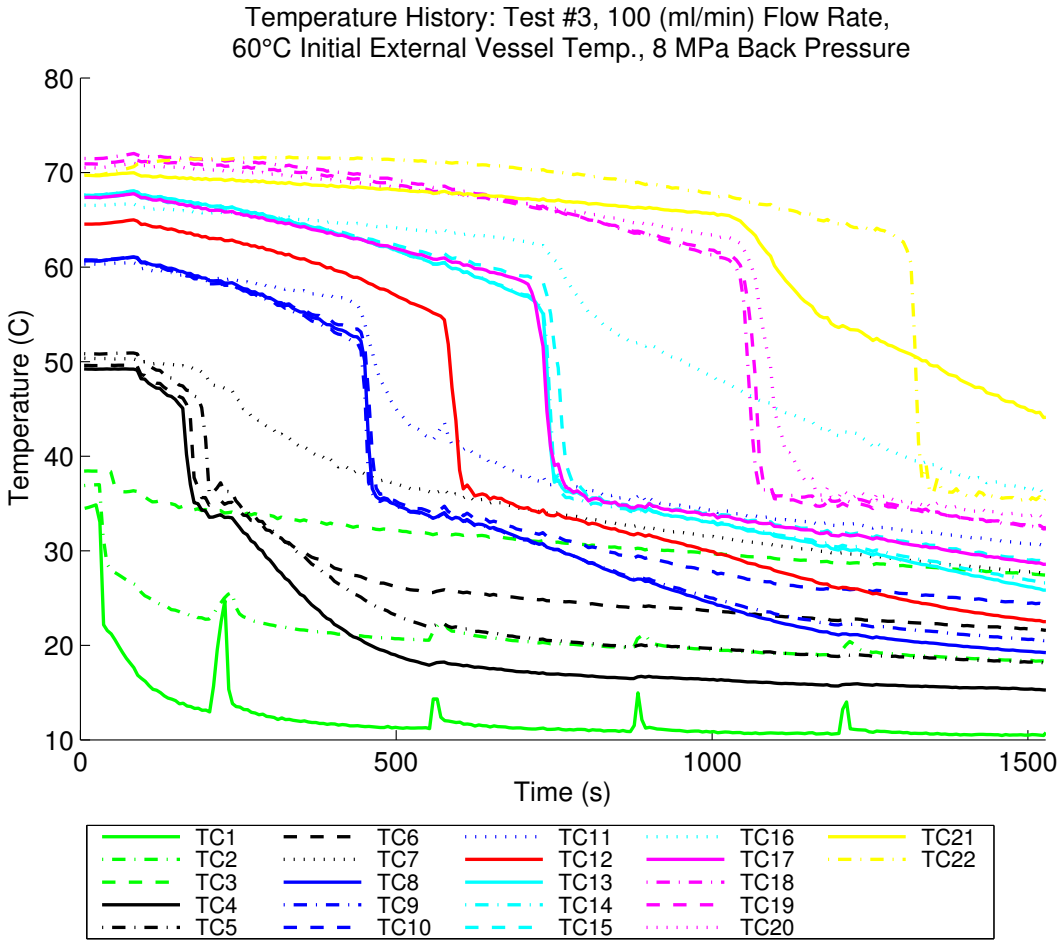

Figure 1.8: Temperature vs time data from twenty-two thermocouples from Experiment 3. The impulses at the injection point were due to the selection of a pump mode that did not implement the pulse free valve operation. There was a slight cessation of flow during pump changeover events that resulted in the fluid in the injection port heating in the steel end cap.

During the course of the experiment the pore velocity, specific heat and density of the two fluids were relatively similar, but the thermal conductivity of the CO_2 fluid ranged from 0.04 to 0.11 W/(m K) while the water had a thermal conductivity range of 0.58 to 0.66 W/(m K).

The experimental data was used to calculate the heat extraction rates of the two fluids. Figure 1.10 shows the heat extraction rates of water (blue line) and CO_2 (red line). The heat extraction rate for the water during the 72-420 second time period of the experiment is significantly higher than that of the CO_2, but the heat extraction rate of the water decreases after the first two pump volumes due to the increased injection temperature. The performance of CO_2 stays somewhat stable despite the fact that the mass flow rate is decreasing during the experiment due to the increase in injection temperature. Since both the water and CO_2 were operated at a similar pressure and volumetric flow rate, it can be assumed that the work

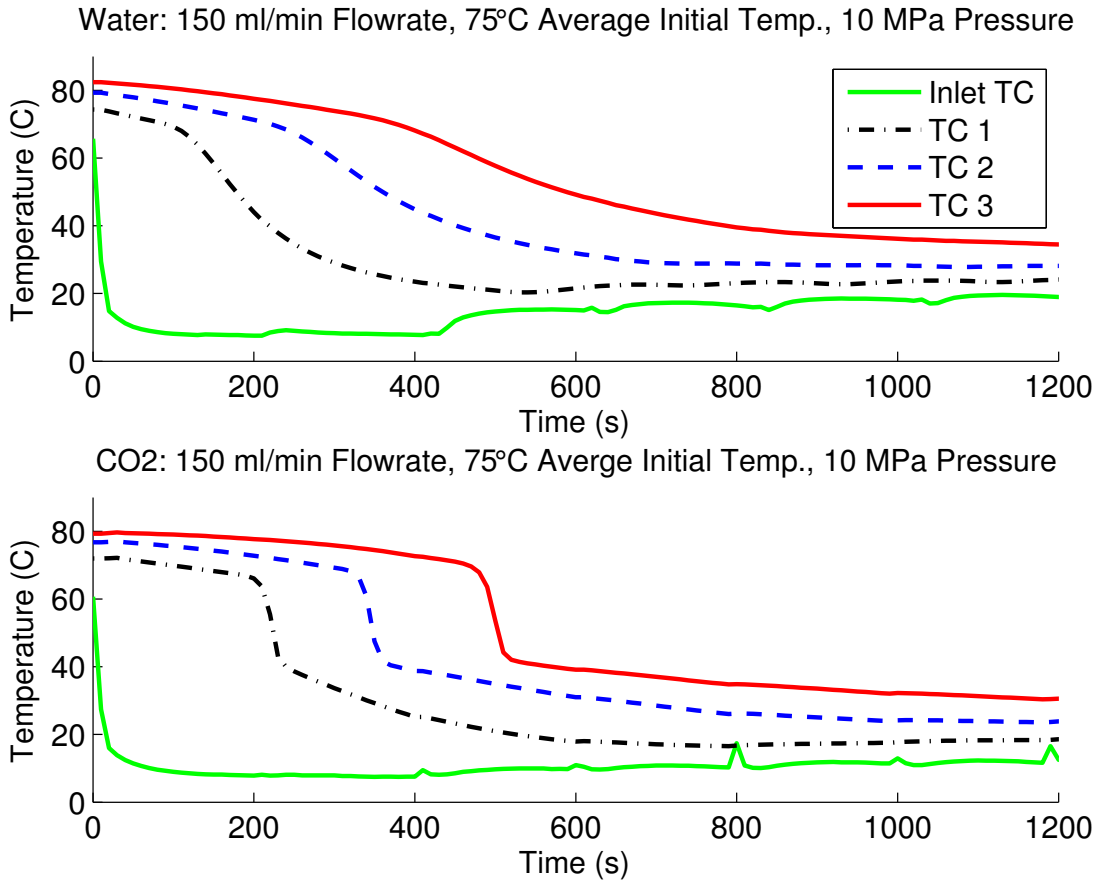

Figure 1.9: Comparison of temperature history data of water and CO_2 as working fluids. Top plot shows a water run and the bottom plot is a CO_2 run. Data is only shown for centrally located thermocouples. (Thermocouple labeling is not consistent with other figures in this paper due to difference in thermocouple array)

performed by the pumps in both experiments was comparable. A complete thermodynamic characterization of the runs would require measurements of the fluid accumulation inside the vessel, which was not recorded for these experiments.

The design of the experiment was primarily intended to produce a data set that could then be used to validate numerical modeling of the use of CO_2 as the working fluid in an EGS reservoir, and was not intended to be directly applicable to full-scale EGS systems. Specifically, the porous medium sample was not designed to replicate the characteristic flow paths that would be expected in a field-scale geothermal system. Despite this, the results can be used to gain insights into the behavior of CO_2 as an EGS working fluid. The experimental results show that CO_2 and water have comparable behavior under a particular set of initial and operating conditions. This result could be viewed as discouraging in the

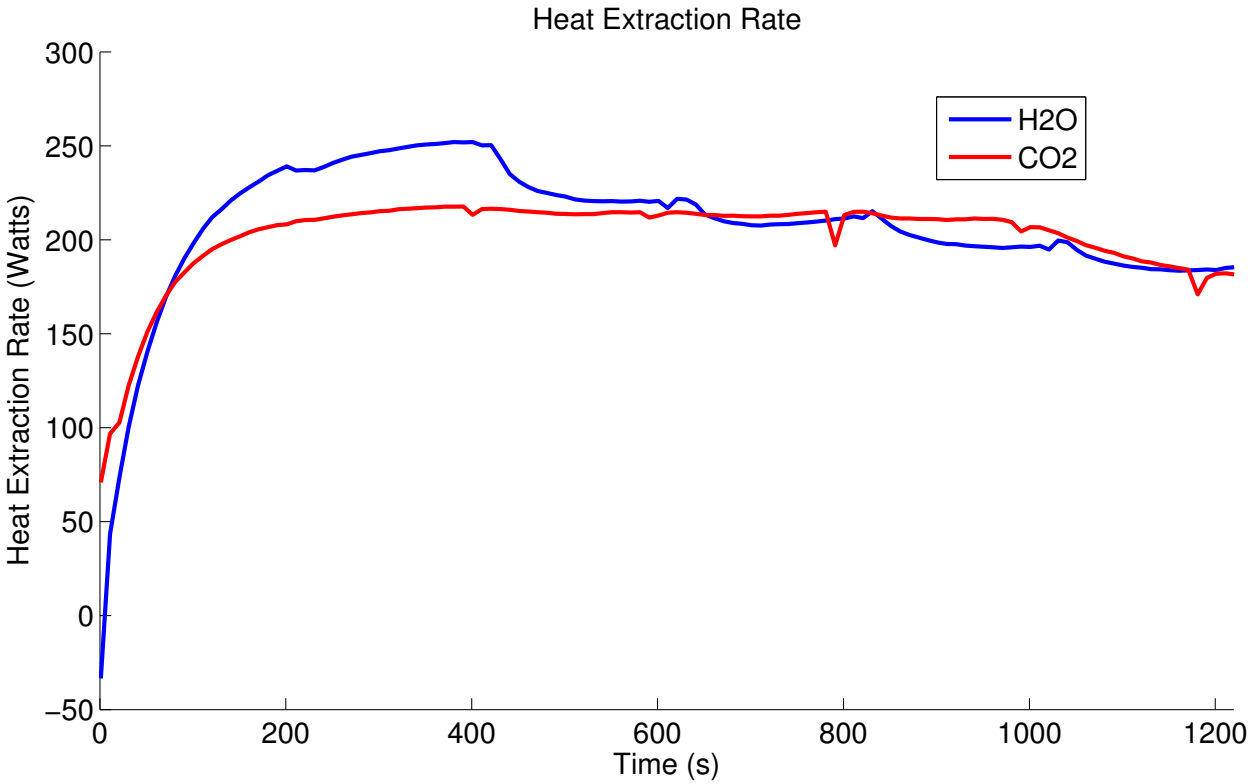

Figure 1.10: Comparison of temperature history data of water and CO_2 as working fluids. Top plot shows a water run and the bottom plot is a CO_2 run. Data is only shown for centrally located thermocouples. (Thermocouple labeling is not consistent with other figures in this paper due to difference in thermocouple array)

context of CO_2 based EGS, but was in line with previous modeling results (Pruess 2007). The greater benefits of CO_2 over water are expected to occur in the 5-spot well geometry that is dominated by radial flow due to the differences in the kinematic fluidity of CO_2 as compared to water. The kinematic fluidity can be used to compare the mass flow rate for different fluids within the same porous medium under the same driving pressure differential and is defined as the reciprocal of the kinematic viscosity, or the ratio between fluid density ρ, and fluid dynamic viscosity μ (kinematic fluidity = ρ/μ).

In a water-based 5-spot EGS system the majority of the driving head loss occurs near the injection well. This is because the lower kinematic fluidity resulting from the colder conditions coupled with the high Darcy flux due to the radial flow pattern around the well require a high driving pressure gradient. This is in contrast to the higher kinematic fluidity CO_2-based system where the head loss is much more evenly distributed across the entire flow path. In the apparatus, the flow is predominately linear along the length of the vessel with small portions of radial flow near the inlet and outlet boundaries. In addition, the thermal energy stored in the large end caps used in the vessel may retard the development of cold

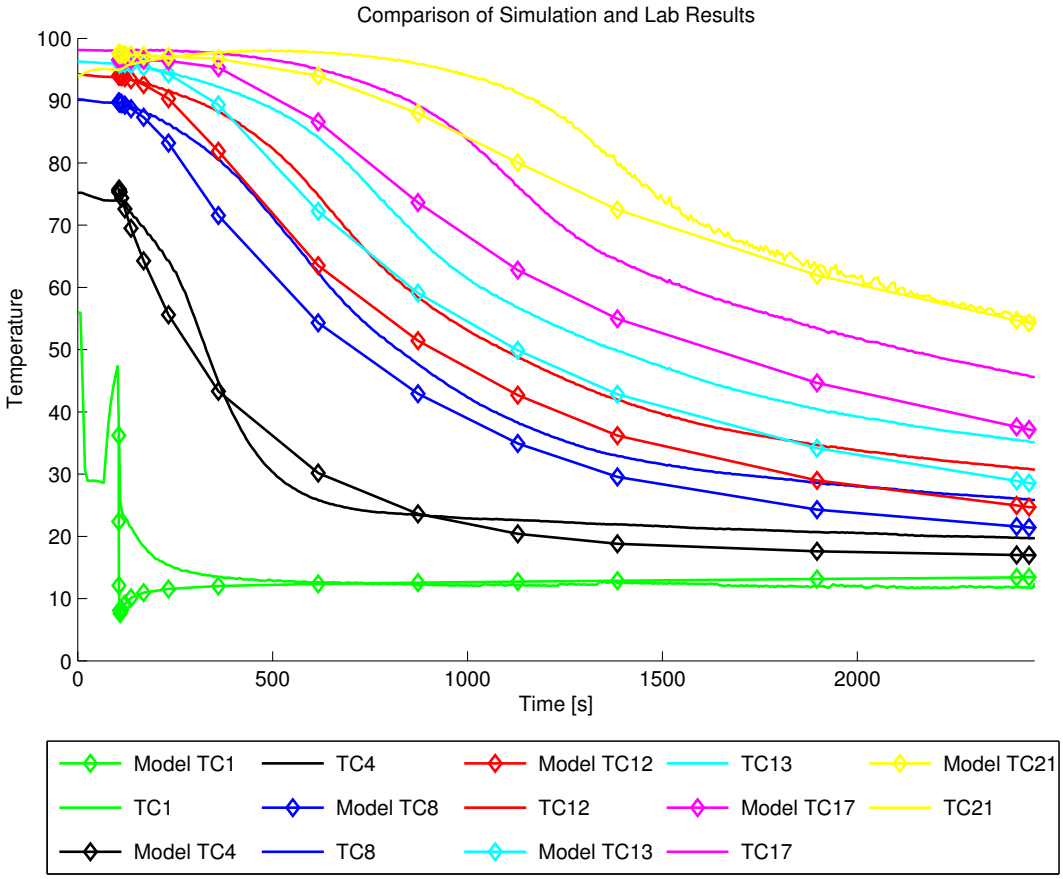

Figure 1.11: Experimental and numerical modeling results for Experiment 1. Experimental data is shown by smooth lines and modeled data by lines with markers

zones near the fluid injection point.

Modeling Results

Custom Matlab scripts were used to generate all of the input files for the TOUGH2 simulation. Values for the input data were read directly from recorded data for the experiment being simulated, including mass flow rate, initial temperature distribution, back pressure, injection temperature and initial effective thermal conductivity of the saturated media. A comparison of simulation and temperature measurements along the central axis of the vessel for Experiment 1 is shown in Figure 1.11.

The simulation data are shown with diamond line markers, while the experimental data is shown without markers. It was difficult to achieve a good fit between the experimental data and the simulation output by manually calibrating the simulation variables. There

are three possible factors for this behavior: 1) the assumption of perfect insulation, 2) difficulties in exactly replicating the boundary conditions in TOUGH2, and 3) changes in thermal conductivity not updated by TOUGH2. The assumption of a perfectly insulated vessel boundary could have a minor effect on the data fit but the effect is not in the correct direction (the modeled systems cools faster than the experimental system), but because of the short timescales in the experiments, it is unlikely to have a significant impact. Imperfectly replicating the boundary conditions may also result in differences, as the steel vessel was assumed to have a uniform temperature, however some small non-uniformities were likely as a result of the heat tape arrangement. The works suggests that the most significant factor affecting calibration of the model to the experimental data may be the manner in which TOUGH2 handles the thermal conductivity of the modeled system.

Heat flux in TOUGH2, conductive and advective, is modeled using the following equation:

$$F_{heat} = \lambda \nabla T + \sum h_\beta F_\beta \tag{1.5}$$

where F_{heat} is the heat flux, λ is the rock formation thermal conductivity under fully liquid saturated conditions, h_β is the specific enthalpy in phase β, and F_β is the advective mass flux of phase β. The value of λ is entered by the user in the TOUGH2 input file and is not updated during the course of the simulation. The assumption that the thermal conductivity of the saturated rock does not change may be valid for relatively incompressible fluids such as water, but it may produce errors for systems where the density of the saturating fluid changes dramatically. For example in Experiment 3, temperatures within the vessel ranged from a minimum temperature of 10.5 °C and a maximum temperature of 72 °C. At operating pressure this resulted in an estimated effective thermal conductivity that ranged from 0.2 W/(m K) at the highest temperature to a thermal conductivity of 1.0 W/(m K) at the lowest. Depending on the relative importance of conduction in the system, the assumption that thermal conductivity is constant may produce results that differ significantly from the observed data.

To see the effect that the choice of thermal conductivity of the CO_2 saturated sand had on the results of a TOUGH2 simulation, two simulations of Experiment 1 were run with two different thermal conductivities: 1 W/(m K) and 0.3 W/(m K). The choice of the two thermal conductivities for the simulation was based on the range of estimated effective thermal conductivities calculated from experimental data for that run. The difference of the temperature history results of these two simulations was calculated at the same locations as the experimental thermocouples by subtracting the results of the simulation of the model with a lower thermal conductivity from the results of the model with the higher thermal conductivity, and plotted in Figure 1.12.

The differences between the two sets of simulation results using different thermal conductivities was variable with time and space. For example at locations near the steel vessel wall, the simulation with the higher thermal conductivity resulted in lower temperatures. Conversely, the temperatures closer to the axis of the sample, including the outlet, were higher with a higher thermal conductivity. For this case, a higher thermal conductivity results in

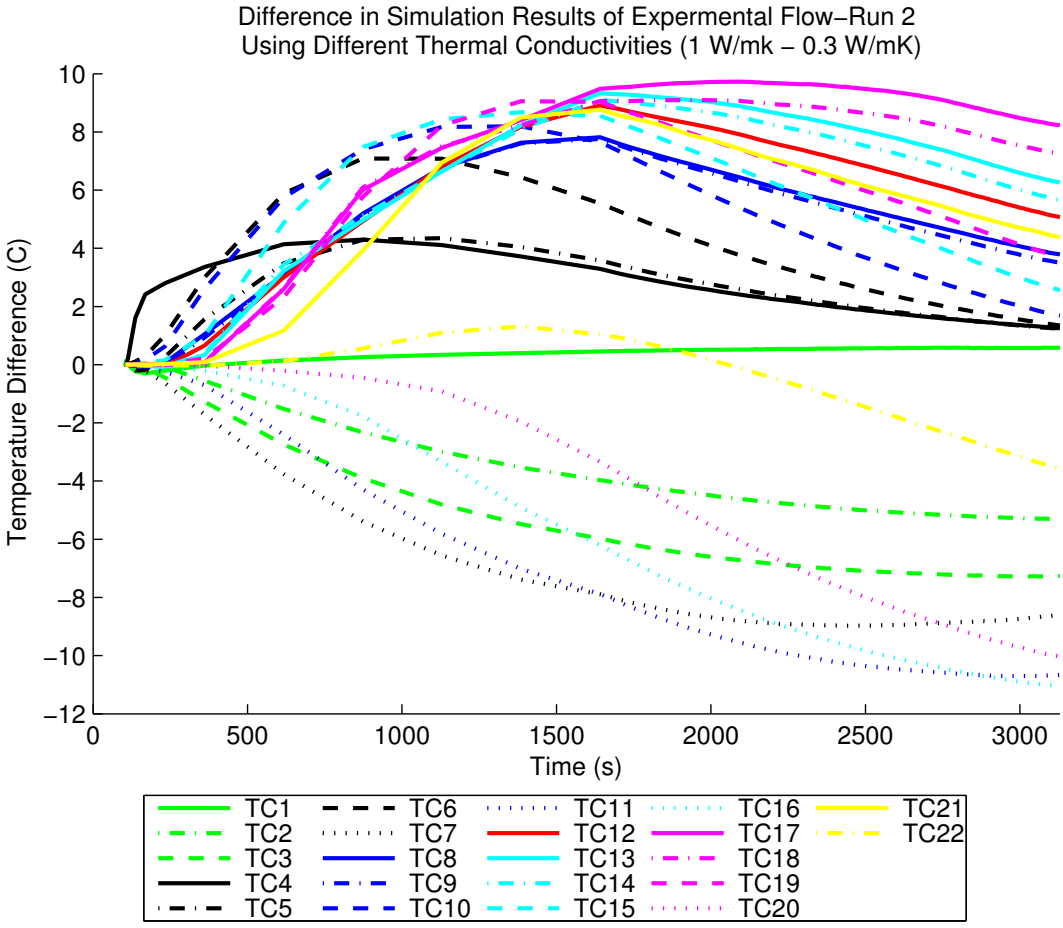

Figure 1.12: Difference between simulation results modeled with two different initial thermal conductivities. Results of run at a thermal conductivity of 0.3 W/(m K) subtracted from the results of a simulation with a thermal conductivity of 1 W/(m K)

higher temperature of the produced fluid throughout the time history of the simulation. The temperature history of the two simulations differed up to 10 °C. The differences in simulation temperature histories that occurred when using different thermal conductivities was within the same order of magnitude as the differences that were found between the model and experimental results. This exercise was not meant to accurately show the error expected due solely to the TOUGH2 assumption of constant thermal conductivity since that task would require extensive intervention to include updated thermal conductivity in TOUGH2 based on the changing state of the CO_2. These results do illustrate the difficulty that might be encountered in choosing a single thermal conductivity value through either manual or automated calibration techniques. Making the effective thermal conductivity a function of the fluid state would be expected to improve the ability to match the experiment data.

With continued interest in CO_2-based geothermal energy production and the reliance on

numerical tools for evaluating its practicality, the results should provide a note of caution for modelers and researchers in this field. A dominant feature of CO_2 as a heat extraction working fluid is the large changes in density that accompany changes in pressure and temperature. While the dynamic density of CO_2 may reduce pumping requirements due to buoyant forces generated as the fluid heats up within the reservoir, the accompanying changes in thermal conductivity should not be ignored when modeling the system. Ignoring changes in thermal conductivity of the CO_2 is not likely to have a large impact on simulations of classical EGS reservoirs that are composed of fractured hot dry rock, since the porosity of these systems is typically low, and the influence of the thermal conductivity of the CO_2 on the effective thermal conductivity of the saturated rock will be small. CPG systems on the other hand are envisioned to be in reservoirs with relatively large porosities on the order of 20% (Randolph and Saar 2011), where changes in the thermal conductivity of the CO_2 could have a significant impact to the heat flow within the reservoir, and the resulting predicted temperature history of the produced fluid.

Altering the TOUGH2 code to include changes in effective thermal conductivity would be difficult since a simple effective thermal conductivity lookup table based on the temperature and pressure could not be employed in a similar manner to how TOUGH2 handles viscosity and density. This is due to the fact that the effective thermal conductivity is dependent on the ratio of thermal conductivity of the fluid to solid, as well as the packing of the media. It would be possible to create a lookup table of effective thermal conductivities indexed by temperature and pressure using the Konii and Smith model (Kunii and Smith 1960) with the experimental sand pack parameters. Creating such a table and adding the functionality to TOUGH2 and ECO2N would be difficult and would only be applicable to sand packs with the same properties as the sample.

Besides altering the TOUGH2 code, including updated thermal conductivity in the simulation could be accomplished by splitting the mesh up into multiple rock domains with separate entries in the input file. The model could then be run forward with a short simulation time step, the output could be used to make new thermal conductivity estimates, and the input file could be updated and the process repeated for succeeding time steps. The thermal conductivity could be updated by using a method such as that described by Kunii and Smith (Kunii and Smith 1960). Using Equations 1.5 and 1.4, and the thermal conductivity of the CO_2 (λ_f) given by lookup tables for the temperature and pressure in the region, the λ_{eff} could be computed for each region in order to update the model between time steps. This method would be cumbersome to deploy, but could be used for simulations where it is determined that the changing thermal conductivity contributes significantly to the temperature response of the system.

1.4 Conclusion

The constructed experimental apparatus, was successful at controlling CO_2 injection, vessel back-pressure, and the measurement of temperature changes at many locations within the

sample. It was found that the process exhibits significant mass accumulation inside the vessel due to increased CO_2 density as temperatures decreased, as would also be expected in a field implementation of this method contributing to CO_2 sequestration. The large changes in density that are associated with changes in temperature may have important implications for the operation of a field-scale EGS system. For example, the temperatures in a geothermal reservoir would drop as energy is produced from the formation, resulting in CO_2 accumulation. If the energy production is decreased or halted, the reservoir will begin to increase in temperature due to heat flux from the surrounding geological formations, which would then result in an increase in pressure. If this pressure increase is not managed, it could result in unwanted fluid migration or geomechanical impacts (e.g., induced seismicity or ground surface uplift).

The relative importance of the conductive versus advective thermal processes in the direction of flow can be seen in the experimental results and corresponds well to the estimated Peclet numbers. The experiments that exhibited sharper transition and steeper thermal fronts corresponded to a higher estimated Pe range than the experiments that had thermal fronts with gentler slopes and smoother transitions. The performance of water and CO_2 were compared using the same operating conditions, and it was found that the heat extraction performance of each fluid was similar in the linear-flow-dominated vessel. This result was expected, and is not applicable to geothermal reservoirs with radial flow patterns.

A representative model of the system was constructed in TOUGH2 using inputs from experimental data, but efforts to achieve a good fit between experimental data and the simulation results through manual calibration were unsuccessful. More knowledge of the conditions at the vessel boundary could improve the model slightly, but concerns remain that the TOUGH2 assumption of constant CO_2-sand matrix thermal conductivity can significantly affect the results of the simulation. Estimates of the effective thermal conductivity of the saturated sampled varied by almost an order of magnitude and this change is not included in the current TOUGH2 code. The differences seen between the experimental results and the simulation results are within the same order of magnitude as seen when different thermal conductivities for the saturated media are chosen for the simulation parameters. The work has shown that when modeling a CO_2 based geothermal reservoir with a numerical tool that does not update the effective thermal conductivity during the simulation, users should exercise caution. Using a conceptual model that is suited for the geothermal reservoir structure, the effective thermal conductivity should be estimated for the range of CO_2 densities that are expected to be encountered in the reservoir operation. The sensitivity of the model should then be tested using the range of effective thermal conductivities, and if results are significantly affected, an alternative modeling method should be found.

Chapter 2

Apparatus for High Flowrate Supercritical-CO_2 Based Extraction Experiments

2.1 Introduction

Concerns about climate change and energy security have spurred a search for a clean, plentiful, and consistent source of energy. Wind and solar based energy sources suffer from lack of consistency and are not capable of providing base load power without advances in large scale energy storage systems. Geothermal energy can provide substantial base load energy, but so far projects have been limited to locations with ideal geological conditions where heat can be extracted economically by water flowing through hot rock. The novel concept of using supercritical CO_2 ($SCCO_2$) as the working fluid in EGS for both reservoir creation and heat extraction was first proposed by Brown (Brown 2000). Numerical simulations of a five-spot well pattern in a hot dry rock geothermal system estimated an approximately 50% greater heat extraction rate using $SCCO_2$ instead of water given the same operating conditions (Pruess 2006).

Besides being a promising geothermal working fluid, supercritical CO_2 has become an important industrial and commercial solvent and an economical tool for oil recovery due to the relatively low critical temperature and pressure, low toxicity, and dynamic physical and chemical properties that can be controlled by varying pressure and temperature. The supercritical state occurs when a fluid is at a temperature higher than its critical temperature and at a pressure that is higher than its critical pressure. The most obvious characteristic of the supercritical state is the lack of a liquid-gas interface with a resulting lack of surface tension. Within the supercritical regime, many properties of the fluid, such as density, viscosity, thermal conductivity, and chemical behavior can change dramatically with relatively small changes in pressure and temperature. While the pressure and temperature based tunability of supercritical fluid properties are attractive for many applications such as extractions and

chromatography, it can also present challenges for fluid handling and process control.

The most commonly used $SCCO_2$, which has a critical temperature of 31.1 °C and a critical pressure of 7.39 MPa, conditions that are relatively easy to achieve in an industrial or laboratory setting. Many of the processes that make use of $SCCO_2$ involve fluid flow through a porous substrate, the efficiency of which can be enhanced by the lower viscosity, higher diffusivity, and relatively high density provided by $SCCO_2$. By varying the pressure and temperature of the $SCCO_2$, the solubility of many compounds in CO_2 can be varied allowing the selective extraction from the source material. $SCCO_2$ has the additional benefits of being non-toxic and non-flammable, and can be separated from the desired extract by evaporation at ambient conditions.

The construction and operation of the laboratory apparatus presented many challenges due, in part, to the highly dynamic nature of $SCCO_2$ as compared to other fluids commonly studied in subsurface flow. The large changes in density of the $SCCO_2$ in response to changes in pressure and temperature as it flowed through the apparatus required special consideration when implementing vessel back pressure control, the measurement of mass flow rate, and delta pressure. Besides the changes in density, the variable viscosity was also problematic for controlling back pressure at the outlet of the vessel. The generally low viscosity, high diffusivity in elastomers, and the organic solvent properties of $SCCO_2$ necessitated careful selection of sealing materials and seal geometry in valves and apparatus plumbing. Special consideration was also required when designing the plumbing in order to alleviate issues caused by expansive cooling of the $SCCO_2$. Existing literature on the construction of a $SCCO_2$ based laboratory flow systems was sparse, and advice from equipment manufacturers inconsistent, therefore many aspects of our apparatus required several iterations before acceptable performance was achieved.

The completed apparatus is capable of continuously flowing temperature-controlled $SCCO_2$ under specified conditions into a large, heated, sand-filled pressure vessel, and measuring temperatures at 23 locations within the sample, the mass rate of fluid injection, the heat input rate, the injection pressure, the vessel outlet pressure, and the pressure difference between the injection and outlet ports of the vessel. The system can be run in a continuous recycling mode, or the produced fluid can be vented to the atmosphere. A series of heat extraction experiments were performed at various back pressures, flow rates, and initial vessel temperatures in order to collect a representative dataset that could be compared to the output of numerical modeling tools.

2.2 Working with Supercritical CO_2

Even though $SCCO_2$ is now commonly used in industrial and commercial settings, the scientific literature lacks details of the practical aspects associated with $SCCO_2$ experiments. The handling, control and measurement of $SCCO_2$ require careful consideration due to the physical and chemical properties of the fluid. $SCCO_2$ is prone to leaking, susceptible to flow blockages, and is difficult to control and measure.

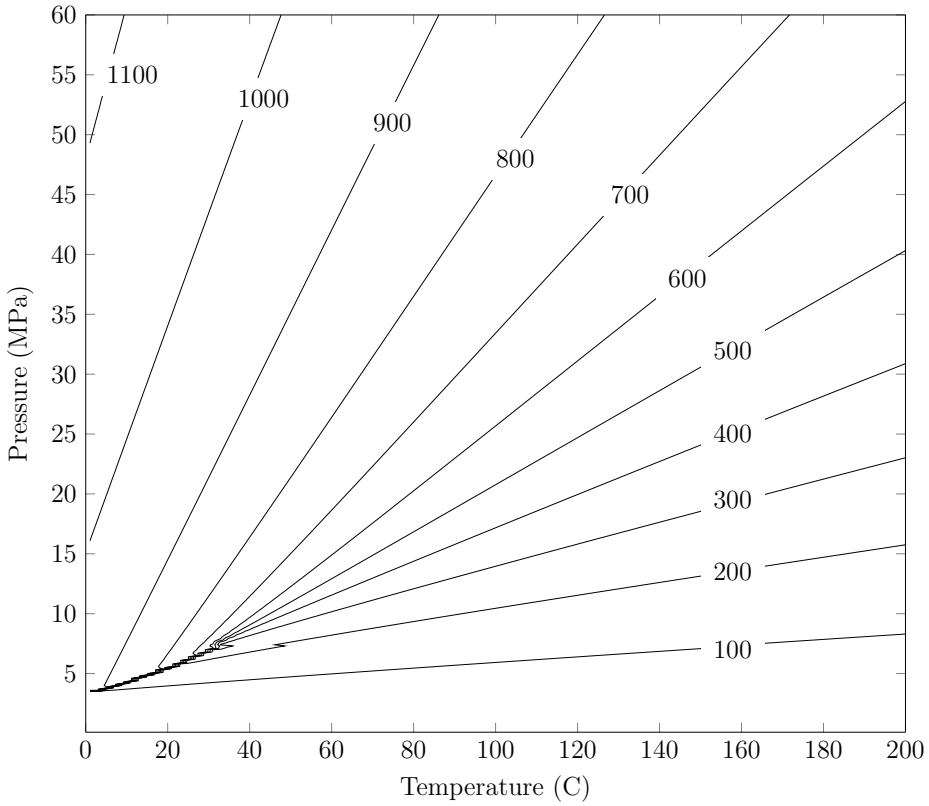

Figure 2.1: CO_2 density in units of kg/m^3. CO_2 exhibits large changes in density due to changes in pressure and temperature. The critical point is located at 31.1 °C and 7.39 MPa. The density generally decreases with temperature and increases with pressure. Large changes in density occur near the liquidus line where the contours of the plot converge below and to the left of the critical point.

The compressibility of $SCCO_2$ is large, and approaches infinity near the critical point as can be seen in the converging contour plots of $SCCO_2$ density in Figure 2.1. The large density variations of the $SCCO_2$ can make it difficult to fill the pumps, cause blockages due to expansive freezing, alter the flow rate through orifices during operation, and can add unwanted variation to delta pressure measurements.

The viscosity of $SCCO_2$ is also highly variable with changes in pressure and temperature (Figure 2.2). The large changes in viscosity that occur within our apparatus during operation can alter the flow rate through orifices, making control of back pressure difficult. The generally low viscosity of $SCCO_2$ can also contribute to fluid leaks from the system to the atmosphere. $SCCO_2$ can diffuse into many elastomers that are commonly used for seals and O-rings, especially when a large pressure differential exists across the material. The diffused $SCCO_2$ can effect the integrity of the material and mechanically damage the seal under certain conditions. $SCCO_2$ sealing problems are compounded by the fact that it can act as

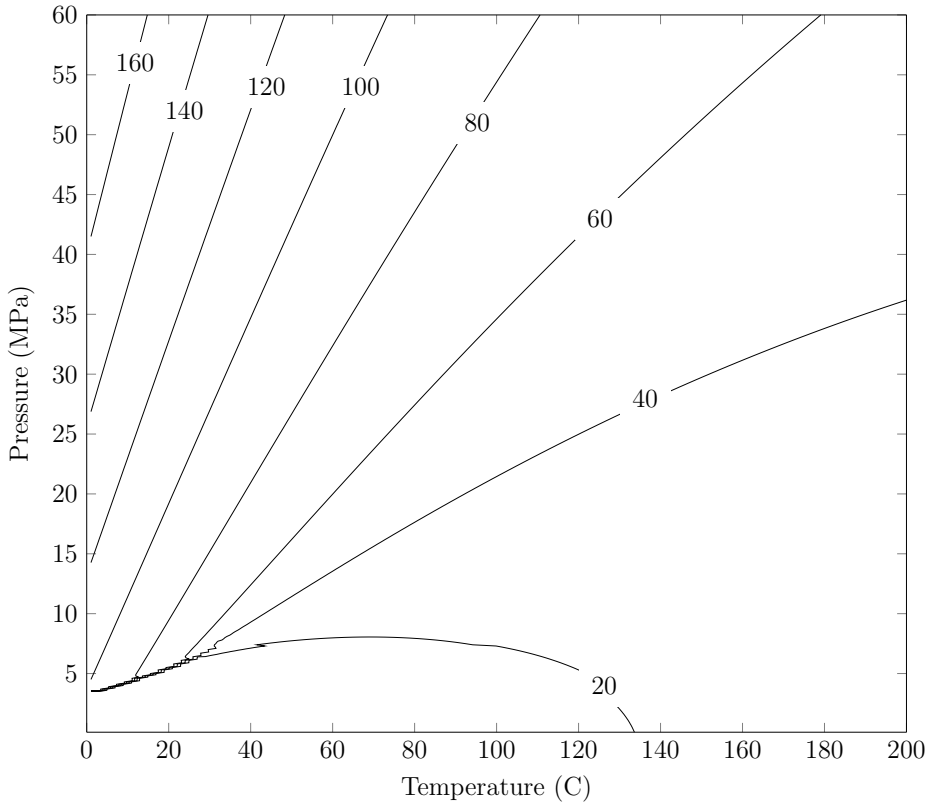

Figure 2.2: CO_2 viscosity in units of millipascal-seconds. The critical point is located at 31.1 °C and 7.39 MPa. The viscosity generally decreases with temperature and increases with pressure. CO_2 exhibits less viscosity variation below the critical pressure and liquidus line.

an organic solvent so that any connection that is dependent on a layer of soluble sealing material is susceptible to leakage. The relatively low vapor pressure of $SCCO_2$ at ambient conditions can also be problematic. At an average ambient temperature of 20 °C, the vapor pressure inside an unheated tank of $SCCO_2$ is about 5752 kPa, which puts a hard lower limit on system pressure when operating in a closed loop mode due to excess expansion at the back pressure regulator, and limits the pressure available to fill the pumps from $SCCO_2$ storage tanks.

Sealing

One of the first things an experimentalist might notice when working with $SCCO_2$ versus water or other common geological fluids, is the effusive nature of $SCCO_2$, behavior that is exacerbated by high temperature and pressures. Seals that can easily hold high-pressure air or even nitrogen will often leak when trying to contain $SCCO_2$. Laboratory experience

has shown us that the best seal is made by a clean, metal to metal contact, as found in common Swagelok® style compression fittings and other conical or tapered seal type systems (Rosenbauer, Bischoff, and Potter 1993). While metal-to-metal seals were found to be superior, tapered thread fittings (NPT) developed leaks and mechanical failures even with the use of Teflon thread tape. While many of the leaks at NPT fittings could be reduced or eliminated by further torquing, often the fitting would be rendered unusable due to galling of the stainless steel at the contact surfaces. It is unknown whether manufacturing defects or quality control were to blame for the bad seals when using tapered thread fittings, but experience has shown that they should be avoided when working with $SCCO_2$.

Figure 2.3: Photo of two perfluoroelastomer (Kalrez®) O-rings damaged by explosive decompression of diffused $SCCO_2$. The top O-ring exhibits a split on the outside circumference, while the bottom O-ring exhibits a split through the entire cross section of the O-ring.

Sometimes metal-to-metal seals are impractical, too expensive, or a required mechanical action precludes their use and a more conventional flexible seal is required. We found that much of the manufacturer published material regarding suitability of seals for $SCCO_2$ was lacking and often wrong. $SCCO_2$ can have a number of varied effects on polymer seal materials such as swelling, stiffening, weakening, breakdown (Davies, Arnold, and Sulley 1999), and blistering (Schremp 1975 pipe article). Ethylene-propylene co-polymers have shown very good resistance to high pressure $SCCO_2$ in tests (Schremp, Roberson, et al. 1975) but we did not make use of the material in our system. Even though fluorocarbon (Teflon, FFKM) based polymers have been shown to be soluble in $SCCO_2$ (Kazarian et al. 1996) and weakened by it (Davies, Arnold, and Sulley 1999), our experience has shown

that they can provide good sealing of $SCCO_2$ in static use where elastomer type seals are required. The primary O-rings on our pressure vessel were constructed of perflouro-elastomer and maintained their seal integrity throughout the life of our experiment. Seal failure did occur when the seals were subjected to large and rapid fluctuations in pressure (Figure 2.3). High-density polyethylene seals were used in the pumps and air operated valves and provided good sealing and abrasion resistance while still requiring periodic replacement.

The thermocouples entered the bottom of the vessel through a two pipes and were sealed with epoxy (Master Bond EP31). Preliminary tests were performed in which stainless steel tubing was sealed with 2 cm epoxy plugs and exposed to 200 °C CO_2 at approximately 27 MPa of pressure on one side and lab air conditions on the other. After a period of time at the test conditions, the plugs failed by sliding out of the tubing. To create a stronger bond between the epoxy and stainless steel the approximately 10 cm long pieces of $\frac{1}{4}$-inch stainless pipe were threaded internally and cleaned before assembly. The pipes were then formed with two opposing 90° bends with a radius of approximately 1 cm. The thermocouples were inserted through the pipes and adjusted to the proper position. A compression fitting cap was then attached to the lab end of the pipes with a small slit machined in it that was just large enough to allow the thermocouples to pass. Finally the pipes were filled with epoxy and the entire assembly was placed under vacuum to remove any air bubbles. The epoxy remained intact and maintained the seal for the entirety of the project.

Pumping

Pumping $SCCO_2$ can be problematic due to the difficulty in quickly and efficiently fillling the pump cylinder with a sufficient mass of $SCCO_2$. In order to produce pulseless flow during pump change over events, at least two pump cylinders are required, and the cylinder must be able to fill and pre-pressurize the fluid before the switch. Due to the relatively low vapor pressure of $SCCO_2$ at ambient conditions, the driving pressure that fills the pumps with $SCCO_2$ directly from the storage tanks is limited. Mounting the pump cylinders below the liquid surface level in the tank increases dispensing pressure, ensures only the liquid phase is present in the pumps, and reduces the time needed to pre-pressurize the pumps before injection. Methods exist to heat the tanks in order to increase dispensing pressure, but the efficiency gains may not be worth the safety risks. To further increase the density of the pump fluid and decrease the chance of vapor formation while at tank pressure, the pump cylinders should be cooled, and a heat exchanger can be added on the inlet side. In our system we used an educator tube $SCCO_2$ tank without a regulator to feed the chilled pump cylinders that were mounted horizontally and close to the floor.

Outlet Pressure Control

For the purposes of operating a $SCCO_2$ extraction experiment there were two practical flow control schemes, maintaining a constant differential pressure across the sample or maintaining a constant mass flow rate into the vessel, both of which require outlet pressure regulation

(Guiochon and Tarafder 2011). Pressure at the outlet can be controlled by a mechanical accumulator (such as a collection pump), a back pressure regulator, or a temperature controlled accumulator. For small total volume of pumped $SCCO_2$, a chilled syringe style collection pump programmed to maintain a constant pressure is an ideal solution for outlet pressure control. Collection pumps and accumulators are limited in size and are impractical for experiments that flow large volumes of $SCCO_2$ through the sample such as in our experiment and require the use of a back pressure regulator. For back pressure regulation we tested both a computer controlled, air-loaded, piston position-sensing type and a multi-orifice, flexible diaphragm type regulators.

An ideal back pressure regulator would allow as much flow as necessary through the valve in order to maintain the desired upstream pressure. Proportional-integral-derivative (PID) back pressure regulators make use of three scalar terms in order to tune the stability and response of the controller to input from a dedicated pressure sensor, in this case an air-load on the piston in response to $SCCO_2$ outlet pressure. The PID-controlled back pressure regulator experienced leakage from the internal seals of the actuating piston and was difficult to tune due to a narrow flow range of the valve and the nonlinear properties of $SCCO_2$. Initially it was difficult to tune the PID regulator to operate satisfactorily across the range of $SCCO_2$ viscosity and density passing through it during a single experimental flow run. In order to increase stability and control we limited the range of $SCCO_2$ density and viscosity as it passed through the regulator by first passing the outlet fluid through a cold water bath heat exchanger. Once tuned, and fed with chilled $SCCO_2$, the PID-controlled back pressure regulator controlled outlet pressure well, with some minor fluctuations due to the mechanical nature of the device.

The PID regulator used perfluoro-elastomer (FFKM) O-rings, for sealing the moving sensing cylinder, which tended to develop leaks over time due to explosive decompression, an example is shown in Figure 2.3. Explosive decompression occurs when a solid material containing diffused $SCCO_2$ experiences rapid depressurization and the material is blistered or ruptured due to the expanding fluid. $SCCO_2$ has been shown to have a significant diffusivity in FFKM (Schremp, Roberson, et al. 1975), and should be avoided in such applications.

After multiple FFKM seal failures with the piston-sensing regulator, we installed a flexible diaphragm type of regulator that featured multiple outlet orifices and a PTFE diaphragm. The flexible diaphragm is loaded with a control pressure on one side, which results in the sealing of the outlet orifices from the inlet. When pressure builds up at the regulator inlet, the diaphragm is pushed away from the sealing surface and the inlet and outlet orifices are opened. The multi-orifice, flexible diaphragm design provides a wide valve coefficient range by unsealing more orifices as the flow rate demand increases, and performed well in our experiments with relatively less variation in pressure than the piston sensing type.

Back pressure regulation also proved problematic due to flow blockages caused by expansive cooling at the outlet of the regulator valve orifice. The extent of cooling is directly related to the pressure differential across the orifice, therefore venting to atmosphere is especially problematic and results in blockages at the orifice. Originally we attempted to limit the magnitude of expansive cooling by using two back pressure regulators in series in order

to lower the pressure in two steps before venting to the atmosphere, but this approach failed due to a lack of volume between the two regulators to buffer the pressure variations. We were able to lessen the pressure drop and resulting freezing issues by using the $SCCO_2$ storage tanks as accumulators that remained at ambient lab temperature instead of attempting to vent to the atmosphere. We used a second back pressure regulator set at a value above the vapor pressure of the ambient temperature $SCCO_2$ as a safety to limit the pressure in the tanks. Using accumulators prevented freezing at the back pressure orifice in most operating conditions except for those at the highest back pressure and flow rate settings. Heat tape has been successfully used to prevent solids from forming blockages at orifices (Friedrich, List, and Heakin 1982).

Mass Flow Measurement

The variable density of CO_2 precludes the use of volumetric-based mass flow measurements unless the state of the fluid is known. Most syringe style pumps can output the current volume, pressure, and displacement rate, which can be coupled with an outlet temperature measurement and a density lookup table to estimate the mass flow rate. Direct mass flow measurements can be made by placing the pumps or source tanks on a scale, or by direct measurement via a coriolis style mass flow meter. Ideally direct measurements of the inlet and outlet mass flow rates should be made to reduce the effect of measurement errors. In our experiment we employed both the lookup method and a coriolis based mass flow transducer after the pumps to compare the measurements. When we were satisfied that the lookup method was accurate, we then moved the mass flow transducer to the outlet of the extraction vessel so that accumulation in the vessel could be recorded. The transducer installation included a remote embedded computer module that processed the meter signals and displayed the mass flow reading on a LCD as well as by analog and pulse width output signals. We used the pulse width output signal into a digital data acquisition system as it had a much faster response time than the other output options.

Delta Pressure Measurements

The pressure readings from gauge pressure sensors mounted at the inlet and outlet of the vessel can be used to calculate pressure differences across the sample that are much greater than the pressure gauge sensitivity. In order to measure smaller pressure differentials, we employed a delta pressure gauge that was hydraulically connected to the inlet and outlet via small diameter tubing. Due to the strong relationship between $SCCO_2$ density and temperature, a vertical temperature and density gradient tends to form in vessels containing $SCCO_2$, even on small scales (Liao and Zhao 2002). We oriented our vessel vertically so that the temperature and gravity driven buoyant forces would be in aligned with the orientation of our flow in order to simplify the dynamics and preserve radial symmetry in our system. The vertical vessel orientation resulted in the static head of the fluid in the delta pressure tubing affecting our delta pressure measurements since the delta pressure connection tubing

was also aligned with gravity. Since the static head of the fluid in the tubing was variable due to the changing pressure and temperature conditions we encased the delta pressure tubing in a cold water bath to impose a constant temperature condition such that the density of the fluid could be estimated using the measured pressure values and the resulting static head could be subtracted from the delta pressure reading. An easier and more stable solution to avoid the contribution of $SCCO_2$ static head to the delta pressure measurement could be achieved using remote seals. Remote seals function by separating the process fluid from the sensor element by use of a sealing diaphragm. The diaphragm is mounted at the location where the measurement is to be taken in contact with the process fluid. The pressure applied to the diaphragm by the process fluid is then transmitted via a second low compressibility fluid located on the opposite side of the diaphragm via tubing to the differential pressure sensing element. This allows consistent measurements to be taken without regard to the temperature or pressure of the process fluid.

Safety

Even though $SCCO_2$ is non-toxic, there are many safety concerns, most importantly suffocation and pressure vessel failure due to over pressurization of system components. Since $SCCO_2$ at ambient conditions is heavier than air, in sufficient quantities it can displace oxygen and lead to suffocation. CO_2 is colorless and odorless, and current occupational health and safety standards limit exposure to 5000 ppm (0.5% by volume of air) during an ten-hour workday during a forty-hour workweek, with 40,000 ppm considered immediately dangerous to life and health (Barsan 2010). Mass and volumetric calculations can be made to estimate the CO_2 concentration and depth of settled gas in the work area in case of complete system depressurization. A stand-alone CO_2 meter was installed in the work area (CO2Meter Inc. eSense II) with an audible alarm and lights that would indicate if the CO_2 levels in the laboratory exceeded 800ppm.

Over-pressurization of system components presents grave danger to life and limb, and can occur due to equipment failures or loss of power, especially when components of the system have been chilled. Pumps and vessels that contain chilled $SCCO_2$ can quickly over-pressurize when chilling is discontinued due to the expansive nature of the fluid. For this reason safety relief valves should be placed throughout the system such that they cannot be shut out by valves. Spring-loaded pressure relief valves are prone to $SCCO_2$ leaks and burst disc types will release all the system fluid when a failure occurs. In our system we have combined the two methods and used burst discs with spring loaded pressure relief valves connected downstream to avoid catastrophic fluid release if an over-pressurization event were to occur.

2.3 Experimental Apparatus

The apparatus diagram in Figure 2.4 is an updated version of the system used to perform CO_2 heat transfer experiments in Chapter 1. The final version of the apparatus con-

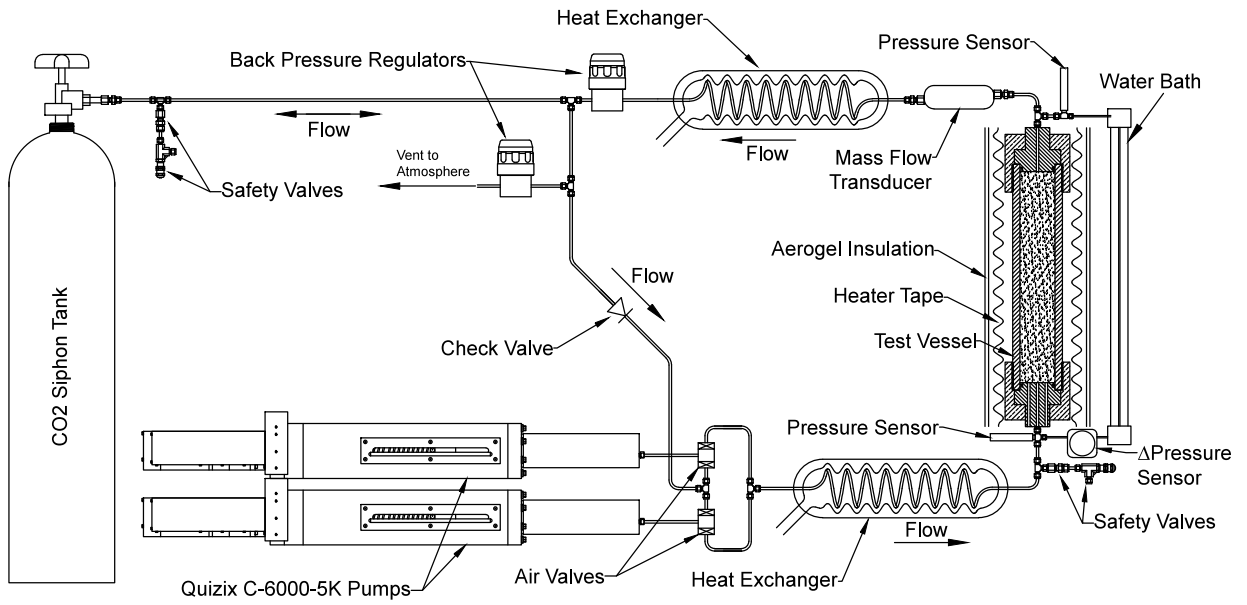

Figure 2.4: Diagram of experimental apparatus. Fluid was supplied by a siphon style CO_2 tank. Fluid was driven by a pair of pumps and fed through air-actuated valves. The fluid was then chilled before it passed into the bottom inlet of the cylindrical pressure vessel that was oriented vertically. A differential pressure sensor was connected hydraulically to the inlet and outlet of the vessel via a temperature-controlled length of tubing that was also oriented vertically. Pressure and mass flow sensors were located at the outlet (top) of the vessel. Pressure in the fluid exiting the vessel was reduced by a back pressure regulator, then passed either back to the pumps via a one way check valve, or returned to the CO_2 storage tank. The vessel was packed with sand and wrapped in heater tape, which was subsequently covered by a fitted aerogel insulation blanket.

sists of a temperature-controlled pressure vessel filled with a porous medium through which temperature-controlled fluid could be introduced by means of high-pressure, high-flow rate pumps (Figure 2.4). The fluid was delivered by a pair of Quizix C-6000-5K pumps, capable of 34.5 MPa and 400 mL/min fluid delivery rate. The pumps can precisely control continuous and pulse-free flow with a resolution of 27.2 nL through the use of constant volume air actuated valves. The injection fluid exiting the pumps was chilled by a water bath heat exchanger before passing into the bottom of the vessel. To quantify the mass of the CO_2 exiting the sample, the injection fluid passed through a Siemens Sitrans MASS 2100-D3 coriolis-style mass flow meter before being chilled by second heat exchanger. The chilled outlet fluid then passed through the back pressure regulator before it entered the pumps via a check valve while excess fluid was collected in the CO_2 storage tanks which were left exposed to the ambient room temperature.

The pressure vessel (High Pressure Equipment Company TOC 31-20) was a hollow type 304 stainless steel cylinder with an inside diameter of 9.1 cm, outside diameter of 12.7 cm,

50.8 cm distance between the type 316 stainless steel end caps secured by 4430 alloy steel caps. Instrumentation and flow access to the interior of the vessel was through three axial passages through the bottom end cap, and one passage through the top. Temperature measurements within the sample were taken by 23 stainless-steel clad type-T thermocouples, which were arranged at various elevations and radii in the sample (Figure 1.2). An Agilent switching digital multimeter connected to a computer recorded the thermocouples voltages and converted them to a temperature reading. All sensor readings and equipment control was managed by a single Labview-based program that allows for accurate time synchronization of experimental data. Combining these functions allowed for a tightly integrated experimental setup, faster data processing, faster experimental turnaround time, and reduced experimental errors.

Because the end caps are massive and heated, the $\frac{1}{4}$-inch inner diameter injection port of the vessel was lined with a length of $\frac{1}{4}$-inch outer diameter nylon tubing through the end cap in order to provide thermal insulation for the injected fluid as it passed through the end cap. The injection port was also fitted with a single thermocouple, mounted where the injected fluid enters the sample space to measure the temperature of the CO_2 as it entered. The outlet passage through the end cap was large approximately, $\frac{3}{4}$-inch in diameter. To avoid large volumetric expansion of the fluid at the outlet passage, a teflon liner was machined to reduce the passage diameter to that same inside diameter as the system plumbing. Both end caps were fitted with thin sintered stainless steel disks to ensure that no media particles could escape out of the vessel.

The sand used in the test sample was from the same batch described in Chapter 1, comprised of silica sand with a very narrow grain size distribution with 83.4% falling between 0.105 and 0.075 mm . The sand was dry-placed in the vessel in multiple lifts with manual tamping with a $\frac{3}{4}$-inch rounded aluminum bar. The vessel was wrapped with five eight-foot lengths of fiberglass fabric-covered heat tape that extended around the exterior of the cylinder and both end caps, with an output of 1248 W each for a total possible output of 6240 W. The heat tape thermal output was regulated by a closed loop-controller that used the feedback from a single thermocouple secured on the vessel exterior. The electrical current supplied to the heat tape was measured by a true RMS ammeter and recorded. Finally the vessel was wrapped in an aerogel insulation jacket and sealed. The aerogel insulation jacket was constructed with a 5 mm thick internal layer of silica aerogel (20-23 mW/(m K) thermal conductivity) reinforced with a non-woven, glass-fiber batting, which was then covered with a reflective Teflon fabric.

2.4 Experimental Results and Discussion

Data was recorded from a total of seven experimental flow runs with the final configuration of the apparatus (Figure 2.4) at various flow rates, back pressures, and initial starting temperatures. The temperature history of a typical experimental run is shown in Figure 2.5. The position of the thermal couples (referred to as TCs in the legend), is shown in Table 1.1

and Figure 1.2 in Chapter 1.

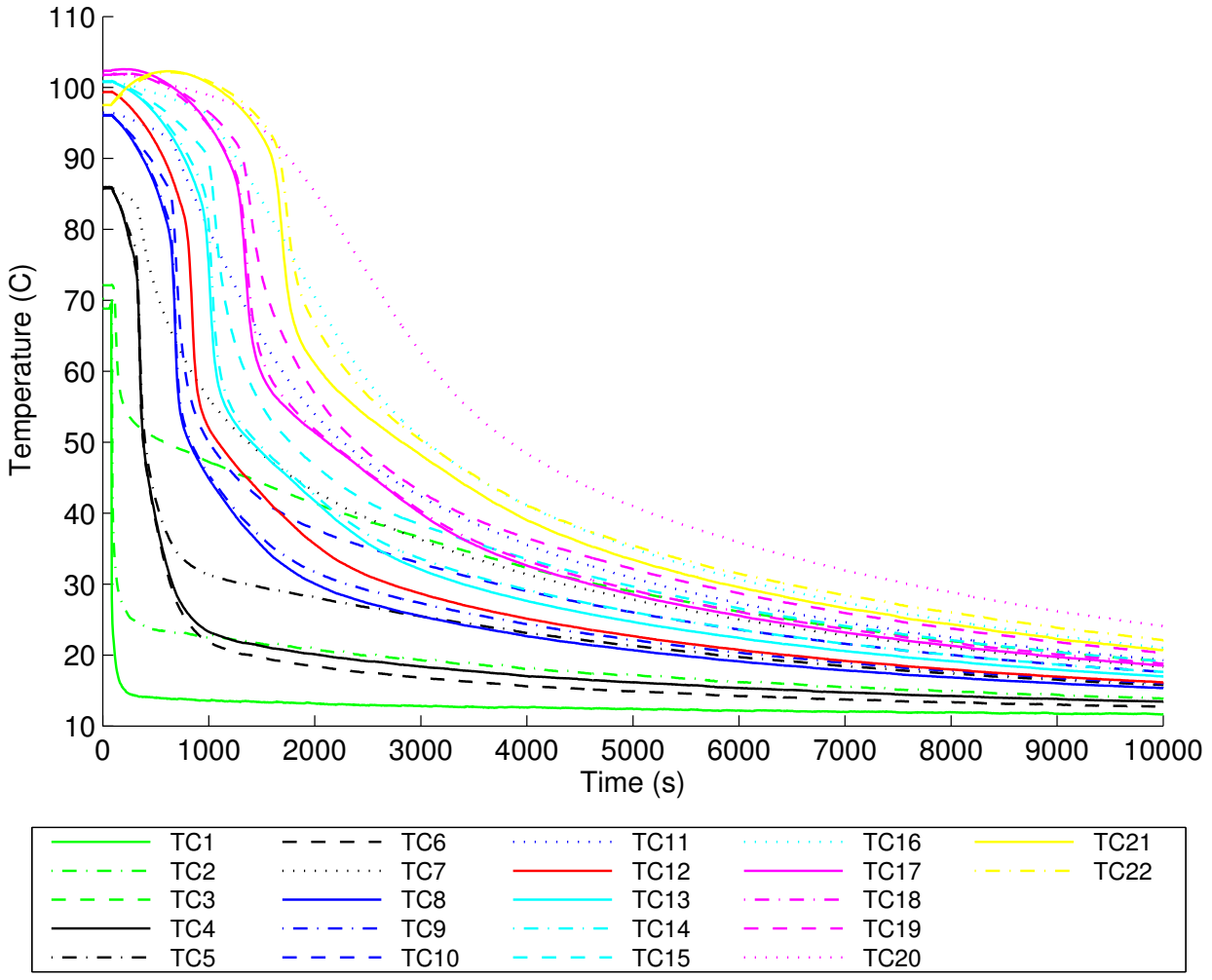

Figure 2.5: Temperature vs time data from twenty-two thermocouples from a typical experimental flow run operated at 100 mL/min flowrate, 108 bar back pressure, and an initial vessel temperature of 100 °C. An initial temperature vertical gradient is present at the beginning of the experiment, with lower temperatures at lower elevations and higher temperatures at higher elevations in the sample. $SCCO_2$ injection initiation can be seen as the steep drop in TC1 temperature (lowest solid green line) at the injection location.

The temperature history data will be primarily used to validate the accuracy of numerical modeling software. An interesting energy balance analysis can be made by coupling the mass input and output rate measurement capabilities of the apparatus with the temperature history at the outlet and inlet and the data acquired from the pump software. Figure 2.6 shows the mass flow rate of injected and produced fluid as measured directly from the mass flow meter at the outlet and by using the lookup method for the inlet. The mass output

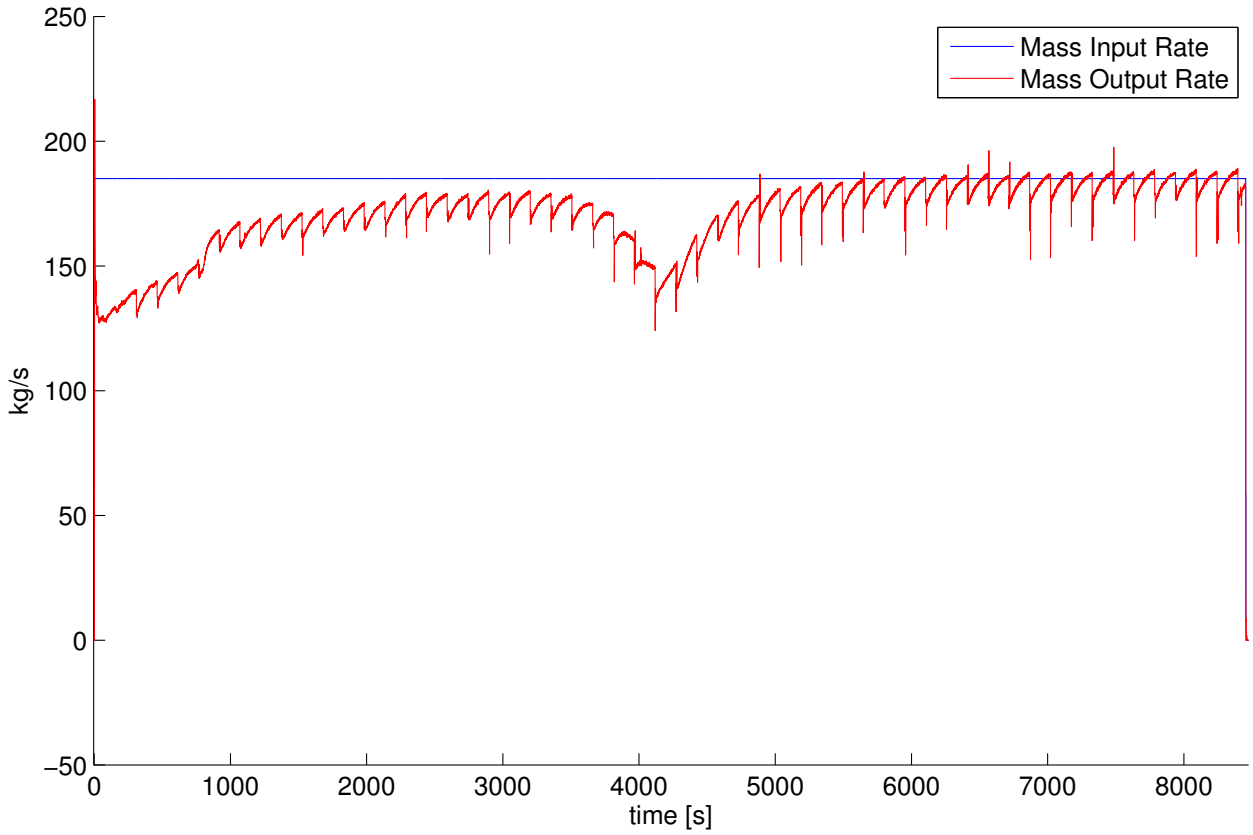

Figure 2.6: Mass flow rates at the outlet and inlet of the vessel. Inlet value based on measured volumetric flow rate, pressure and a density look-up table. Outlet value based on mass flow meter readings.

signal varies due to the mechanical nature of the back pressure regulator as the orifice opens and closes. The dip in the output rate in the middle of the experiment is unexplained at this time, but indicates a period of increased $SCCO_2$ accumulation within the vessel. This dip in mass output has been seen in all of our experimental flow runs, and our modeling studies have shown a similar but less dramatic signal in the simulation output.

The work performed by the pump (W_p) on the system can be calculated using the relationship:

$$W_p = F_{V,p}P \tag{2.1}$$

where $F_{V,p}$ is the pump volumetric flow rate, and P_p is the pressure inside the pump. The change in internal energy of the system dU_{sys} can be described by:

$$dU_{sys} = dH_{in} - dH_{out} - \delta Q + \delta W_p \tag{2.2}$$

where dH_{in} and dH_{out} are the enthalpy flux into and out of the system respectively, and δQ is the heat loss to the lab environment.

To calculate the enthalpy fluxes, the mass flux in ($F_{m,in}$) and the mass flux out ($F_{m,out}$) are multiplied by the specific enthalpy h (in units of J/kg) of the fluid that is found via lookup tables based on the corresponding pressure and temperature. Combining Equation 2.1 and 2.2 and the enthalpy calculation results in the expression:

$$dU_{sys} = F_{m,in}h_{in} - F_{m,out}h_{out} - \delta Q + F_{V,p}P \tag{2.3}$$

By applying this relationship to experimental flow runs that began with the same initial internal energy, we can compare the rate of change of the internal energy of the system based upon the rate of work added to the system by way of the injection pumps. This analysis was performed on three of the experiments (numbers 4, 5, and 6) which shared the same initial pressure and temperature, and therefore had the same initial internal energy. Figure 2.7 shows the result of this analysis. It can be seen in the plot that during the increased mass accumulation phases of the experiments the system is actually increasing in energy as shown by the negative energy loss values. This analysis demonstrates the variability of a $SCCO_2$ based extraction system attributed to the choice of mass flow rate, and the importance of understanding a system's response when choosing operational parameters.

The differences in heat extraction performance of the system K_{sys} under different operating conditions can be shown by comparing the heat extraction rate to the work input rate as a ratio:

$$K_{sys} = \frac{F_{m,out}h_{out} - F_{m,in}h_{in}}{F_{V,p}P}. \tag{2.4}$$

A plot comparing the heat extraction performance of the same three experimental runs can be seen in Figure 2.8. The results show that the performance of the system is highly dependent on the operating parameters chosen. Using a lower mass flow rate that requires less pumping work is more efficient for extracting heat from the system than a high mass flow rate. Depending on the goals and constraints of a $SCCO_2$ heat extraction project, such information is vital to planning and operation.

2.5 Conclusion

Despite the challenges in working with $SCCO_2$ in the laboratory, materials and methods were identified that enabled data collection of the temperature history and the thermodynamic behavior of the system under different operating conditions. The work has shown that metal-to-metal tapered seals offer the best performance for containing $SCCO_2$ and tapered pipe thread fittings often fail. It was found that when moving seals are required that high-density polyethylene-based seals offered excellent sealing performance and a reasonable work life. Avoiding the use of perfluoroelastomer-based seals is highly recommended, especially in applications that subject the material to high pressure differentials and rapid pressure changes.

The control problems associated with the extreme compressibility of $SCCO_2$ can be addressed by careful management of pressure drops along the process path by way of temper-

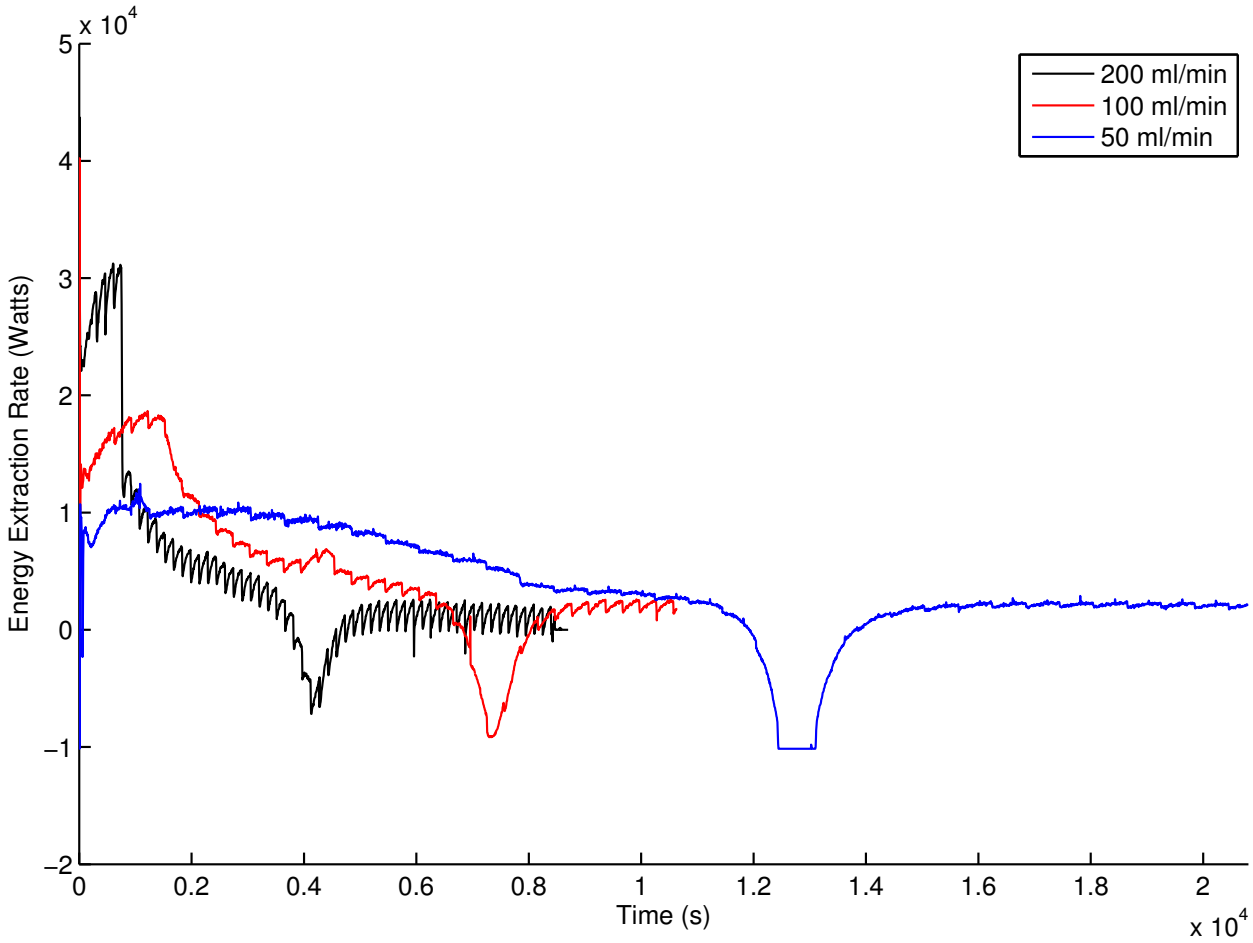

Figure 2.7: The internal energy loss of the system under three different flow rates.

ature control and the use of accumulators between pressure reducing valves. The work has shown that the compressibility of $SCCO_2$ can introduce many sources of error to measurements such as mass flow and pressure drops. Direct measurement by way of coriolis-based mass flow transducers is preferable to pressure- and temperature-based lookup methods as it introduces fewer sources of error and uncertainty. The use of the process fluid as a method of transmitting pressure information to a pressure transducer should also be avoided as the state of the fluid may introduce error to the measurement. When making remote pressure measurements that are often required when measuring small pressure differentials across distances, we recommend the use of remote seal devices that contain a low compressibility working fluid.

$SCCO_2$ presents some serious safety concerns including suffocation due to fluid escape and overpressure conditions due to control errors or loss of cooling. The volume of the workspace should be sufficient to avoid suffocation if all process fluid is released, and a CO_2 detector should be employed that will produce an audible and visual alarm when dangerous

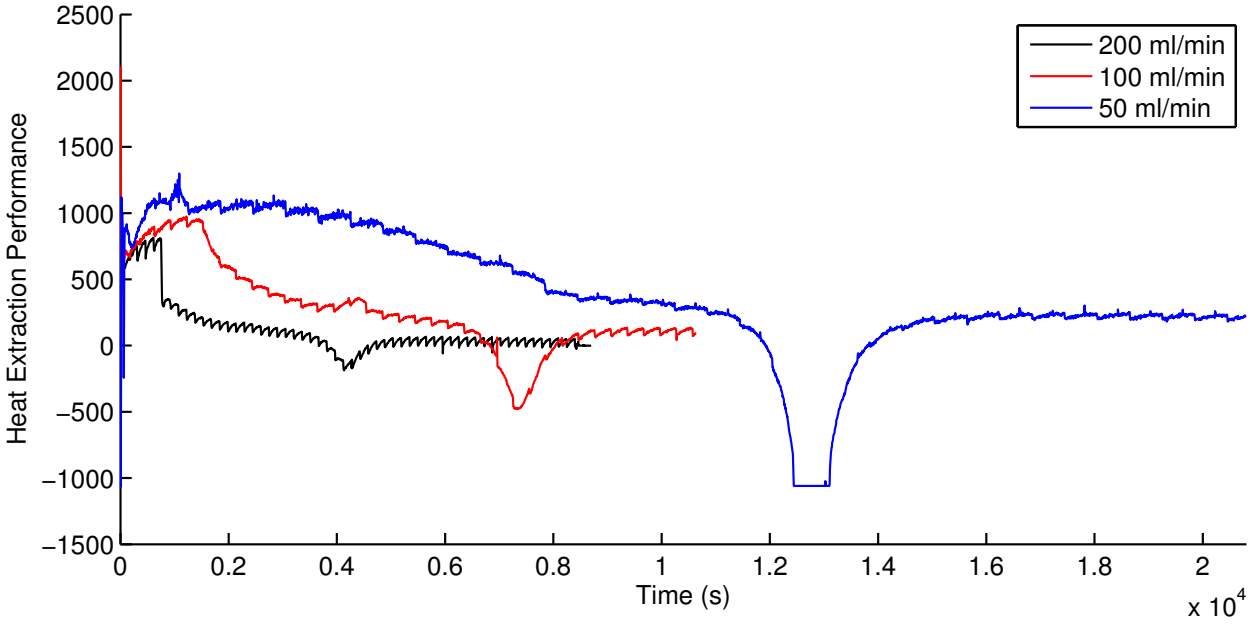

Figure 2.8: The heat extraction performance of three experiments operated under different flow rates.

concentrations of CO_2 are present. Calibrated burst disks followed by a spring loaded pressure relief valve downstream should be used to prevent total loss of process fluid due to an overpressure event.

The assembled apparatus produced data that can be used for CO_2-based porous media flow model validation at conditions that are applicable to field scale geothermal energy production. Our data illustrates the dynamic behavior of heat extraction from a porous sample by flowing $SCCO_2$, especially in terms of non-linear mass accumulation. Our analysis of the data shows that the energy extraction rate and the heat extraction performance of a $SCCO_2$ system is highly dependent on the mass flow rate of the injected $SCCO_2$.

Chapter 3

Numerical Modeling of the Heat Transfer in CO_2 Core Flood Experiments with ECO2N V2.0

3.1 Introduction

Numerical modeling tools are necessary for studying, planning, and operating geologic-based CO_2 sequestration and CO_2-based geothermal energy projects. Project viability and safety is dependent on the results of computer simulations of heat and mass flow in porous media, so model validation is an important concern. Models can be tested against closed form solutions, compared with other models (Pruess et al. 2004), or ideally they can be compared with measurements of actual physical systems. The data sources for validation either come from field data, that is usually sparse in space and time and very expensive, or laboratory experiments, which are often denser in space and time but usually lack the proper scaling. Many of the properties of CO_2 that are important to the relevant flow processes vary dynamically and significantly with temperature and pressure, therefore closed form solutions are limited in scope and usefulness (Narasimhan and Lage 2005) and sparse data sets can leave many uncertainties after analysis is complete.

Previous experiments collected data from a specially constructed apparatus that injected cold CO_2 into a heated porous sample and compared the results to a numerical model of the system implemented in the TOUGH2 family of code using the ECO2N equation of state module (Chapter 1). TOUGH2 is a general purpose non-isothermal, multiphase, multicomponent fluid flow simulator for porous and fractured media developed by Karsten Pruess and others at Lawrence Berkeley National Laboratory (LBNL) (Pruess 2004). The experimental apparatus was capable of recording temperature data at high frequencies in time and space, as well as pressure at the inlet and outlet and mass flow at the inlet. In past experiments it was impossible to achieve a reasonable match between experimental and model results by trial and error. Our analysis found that the constant effective thermal

conductivity of the saturated medium assumption used in TOUGH2/ECO2N was a likely source of error in the model results.

Since the initial experiments were performed, the ECO2N module has been updated and optional code (TCSUB) created that allows for more accurate effective thermal conductivity modeling (Pan et al. 2015). Using an updated version of our apparatus (Chapter 2) a new set of data was captured that includes the mass flow at the outlet of the vessel and was used to perform the first comparison of the results of the new thermal conductivity modeling code to measured data. This chapter presents the results of the experimental and numerical studies and examine what effects the updated thermal conductivity model has on the simulation accuracy.

3.2 Laboratory Core Flood Experiments

Experimental Apparatus

Temperature, pressure, and flow rate measurements were taken with the updated experimental apparatus described in Chapter 2 (Figure 2.4). The experiment was designed to generate data for numerical model validation purposes by careful implementation of boundary conditions, the layout and density of temperature measurements, and the selection of experimental parameters such as flow rate and porous media grain size. The goal was to exert as much control over the system as possible, and when not possible, to measure those conditions accurately in space and time. The inlet is controlled as a constant enthalpy flux boundary by means of the computer controlled pumps and a laboratory chiller. The outlet is controlled as a constant pressure boundary condition by means of a back pressure regulator. Constant pressure and constant mass flux boundary conditions are easily implemented in a TOUGH2 model. The vessel was insulated by a custom fabricated aerogel insulation blanket in order to impose a relatively low heat flux at the exterior surfaces of the vessel.

Porous Core Sample & Operating Parameters

The core sample consisted of dry-packed, well sorted, spherical shaped quartz silica sand. The shape and sorting of the media was chosen to further simplify the our system. Many conceptual models of porous media flow make use of a packed bed of spheres to represent the solid matrix. The sample was prepared from F95 Ottawa silica sand (U.S. Silica), shown in Figure 3.1. Sieving and washing resulted in a narrow grain size distribution. 4.9489 kg of prepared sand was packed into the mounted vessel in 15 separate lifts with manual tamping with a rounded aluminum rod between lifts. The porous sample properties are listed in Table 3.1. The porosity was calculated from the packing weight, vessel volume, and quartz density.

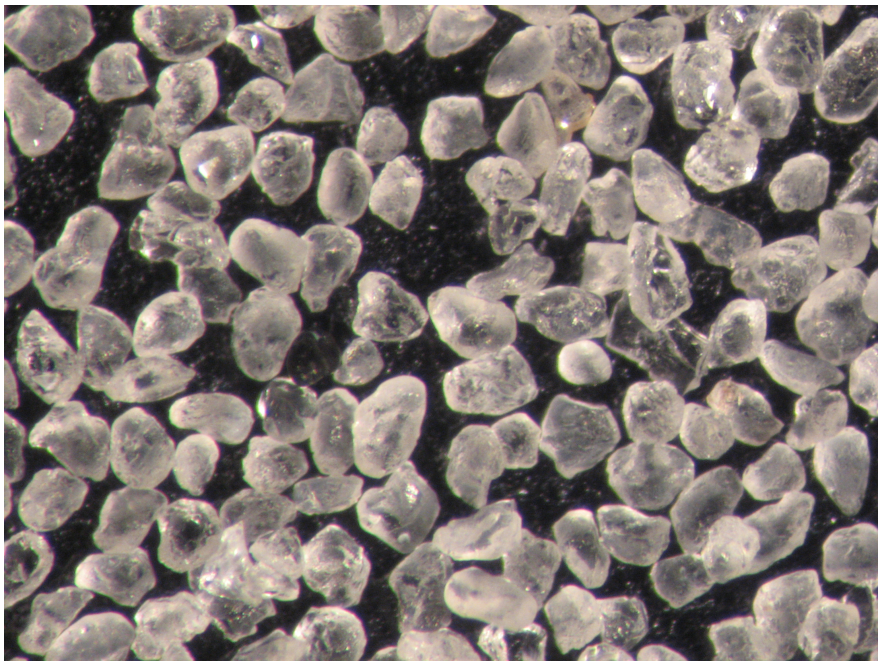

Figure 3.1: Photo of sorted Ottawa sand.

Scaling Considerations & Operating Parameters

The operating parameters were selected to ensure that the experiment was within the mass and heat flow regimes that are applicable to TOUGH2 and full scale CO_2 geothermal projects. TOUGH2 is limited to simulating mass flow that lies within the Darcy flow regime which corresponds to a system in which the viscous forces are dominant over the inertial forces. To ensure that the experiment is operated in the Darcy flow regime the Reynolds number of the system should be low, ideally less than 1 but never more than 10 (Zeng and Grigg 2006). The Reynolds number of the fluid flow through the medium can be calculated using the expression for spherical packed beds (McCune and Wilhelm 1949).

$$\mathrm{Re} = \frac{v_s \rho D}{\mu \phi}, \tag{3.1}$$

where v_s is the Darcy velocity or specific discharge, ρ is the fluid density, D is the particle diameter, μ is the dynamic viscosity, and ϕ is the porosity of the sample. The Darcy velocity is defined as $v = \dot{V}/A$, where A is the cross sectional area of the vessel, and $\dot{V}$ is the volumetric flow rate across the surface of the area. To find an upper bound of the system Reynolds number (Re_{max}) it is assumed that it will occur shortly after fluid flow has initiated when the colder and denser injection fluid displaces the less dense hot fluid already present in the sample. At later times the fluid flowing within the sample will become more dense and more viscous thereby lowering the Reynolds number as the temperature decreases. A further assumption is that there is no initial mass accumulation in the vessel and that the

Porous Core Properties	
Total Core Length	$\mathrm{L} = 50.8\,\mathrm{cm}$
Cross Sectional Area	$\mathrm{A} = 6.54 \times 10^{-3}\,\mathrm{m}^2$
Crystalline Quartz Density	$\rho_\mathrm{R} = 2650\,\mathrm{kg/m}^3$
Crystalline Quartz Specific heat	$\mathrm{C_R} = 830\,\mathrm{J/(kg\,K)}$
Crystalline Quartz Thermal Conductivity	$8\,\mathrm{W/(m\,K)}$
CO_2 Saturated Sand Effective Thermal Conductivity Range	0.22-1.0 $\mathrm{W/(m\,K)}$
Permeability	$\mathrm{k} = 9.3 \times 10^{-10}\,\mathrm{m}^2$
Porosity	$\phi = 43\%$
Mean Grain Size $\mathrm{d_{50}}$	$\mathrm{d_{50}}$ 0.105 mm

Table 3.1: Porous core thermal, physical, and hydraulic properties.

volumetric flow rate of the hot fluid in the vessel can be related to the volumetric flow rate of the cold fluid from the injection pump ($\dot{V}_p$) by the ratio of their densities: ρ_p/ρ_v. Assuming no accumulation, the Darcy velocity within the sample can be related to the volumetric flow rate of the injection pump by the expression

$$v_s = \frac{\dot{V}_p \rho_p}{A \rho_v}. \tag{3.2}$$

Combining Equations 3.1 and 3.2, an estimate for the maximum Reynolds number (Re_{max}) can be expressed as

$$\mathrm{Re}_{max} = \frac{\dot{V}_p D \rho_p}{A \phi \mu_v}, \tag{3.3}$$

where μ_v is the dynamic viscosity of the hot fluid in the vessel at injection initiation.

The ECO2N module is used to model CO_2-based geothermal systems and sequestration projects often operate on the kilometer scale, while the largest dimension of our sample is less than a meter. To compare the heat transfer dynamics, the Peclet number of the two systems can be compared which gives us a measure of the importance of advection driven heat transfer over the conduction driven heat transfer. The Peclet number can be expressed as the ratio of the time required for both processes to pass across the length scale in question, or conduction time over advection time.

$$\mathrm{Pe} = \frac{t_{cond}}{t_{adv}} = \frac{\frac{L^2}{D_{th}}}{t_{ad}} = \frac{L^2}{D_{th}(\frac{L}{V_p})} = \frac{L V_p}{D_{th}} \tag{3.4}$$

In Equation 1.1 t_{cond} is the characteristic thermal conduction time, t_{ad} is the characteristic fluid advection time, D_{th} is the thermal diffusivity, L is the characteristic length, and V_p is

the pore velocity. This formulation ignores the thermal retardation factor effect on thermal advection and instead compares the bulk stagnant thermal conduction time to the fluid mass advection time. This assumes a null specific heat capacity of the sand for advection. The bulk pore velocity for the experiment was oriented in the vertical direction with the fluid injected into the bottom of the vessel and was produced at the top. All the Peclet numbers calculated and referenced in this paper were for the vertical direction. Heat transfer in the radial direction from the heated stainless steel vessel walls toward center of the sample was largely conductive/dispersive due to the lack of imposed flow in the radial direction. The bulk stagnant thermal conduction time was found by estimating the thermal diffusivity of the sand and CO_2 at experimental conditions

$$D_{th} = \frac{\lambda_{eff}}{\rho_{avg} C_{p,avg}} \tag{3.5}$$

where λ_{eff} is the estimated effective thermal conductivity of the CO_2-media matrix, ρ_{avg} is the volumetric average density of the CO_2-media matrix, and $C_{p,avg}$ is the average of the specific heat of the CO_2-media matrix. Assuming the thermal diffusivity and effective thermal conductivity of a field-scale system and our laboratory sample are similar, it can be seen that to achieve a field-scale Peclet number in the laboratory setting requires that the pore velocity be scaled inversely to the ratio of the field and lab length scales. The sample length in laboratory apparatus is approximately on the meter scale, and field geothermal systems typically are on a kilometer scale (Wit and Wilen 2010). Pore velocities of engineered geothermal systems can be on the m/h scale (Aquilina et al. 2004), or about 1×10^{-4} m/s. A pore velocity on the scale of 0.1 m/s would be required in the vessel in order to obtain the same magnitude Pe number between the field and lab systems, yet such a high velocity would result in a Reynolds number outside of the Darcy regime. Since the Reynolds number and pore velocity will change in time and space during an experiment, a characteristic value can be calculated based on the mass flow rate of the pump and a vessel temperature equal to the mean value of the injection fluid and initial vessel temperature. The maximum Reynolds number and the average pore velocities were calculated for various flow rates and back pressures are listed in Table 3.2 assuming an injection temperature of 11 °C and an initial vessel temperature of 100 °C and no mass accumulation in the vessel.

All of the estimated Reynolds values are below 10 while only the lower flow rates at the higher pressures result in numbers close to 1. The estimated pore velocities are not high enough to fully offset the difference in length scales between the lab experiment and field operations when considering the heat transfer regime. Though not ideal, the choice of flow rates and back pressures strike a compromise between low Re numbers and reasonably high pore velocities.

Experimental Results

Five single-phase CO_2 experiments were performed under the conditions listed in Table 3.2. The temperature data from the twenty-two thermocouples (ignoring the redundant

Operating Condition	Re_{max}	Re_{avg}	$V_{p,avg}$ (m/s)
200 ml/min pump flow rate			
108 bar	5.5	5.5	5.1×10^{-3}
82 bar	5.5	5.5	2.8×10^{-3}
100 ml/min pump flow rate			
108 bar	2.5	1.9	1.3×10^{-3}
50 ml/min pump flow rate			
147 bar	1.1	0.63	0.5×10^{-3}
108 bar	1.3	0.96	0.7×10^{-3}

Table 3.2: Estimated maximum Reynolds number, average Reynolds number and average pore velocity for experimental flow rates and back pressures.

thermocouple) from the experimental flow runs are shown in Figures 3.2-3.6. Before injection initiation a vertically oriented thermal gradient is present in the vessel with the highest temperature at the top of the vessel and the lowest temperatures at the bottom. Injection initiation can be seen as the temperature at the sample inlet (solid green line) drops shortly after time zero. The relative importance of convective and advective driven heat transfer can be seen in the temperature plots by the steepness of the temperature curves at the time that the temperature front passed that location. Advectively dominated heat transfer can be seen in the near vertical curves and sharp transitions of temperature plots of experiment numbers one and three (Figures 3.2 & 3.4) which correlates to the high estimated pore velocities (Table 3.2). Experiment numbers two and five, which had the lowest estimated pore velocities, exhibit less steep curves and smoother transitions (Figures 3.3 & 3.6) that are characteristic of less advectively dominated heat transfer. Experiment number four exhibits a near vertical temperature slope and smooth transitions (Figure 3.5) that correspond with the intermediate estimated pore velocity.

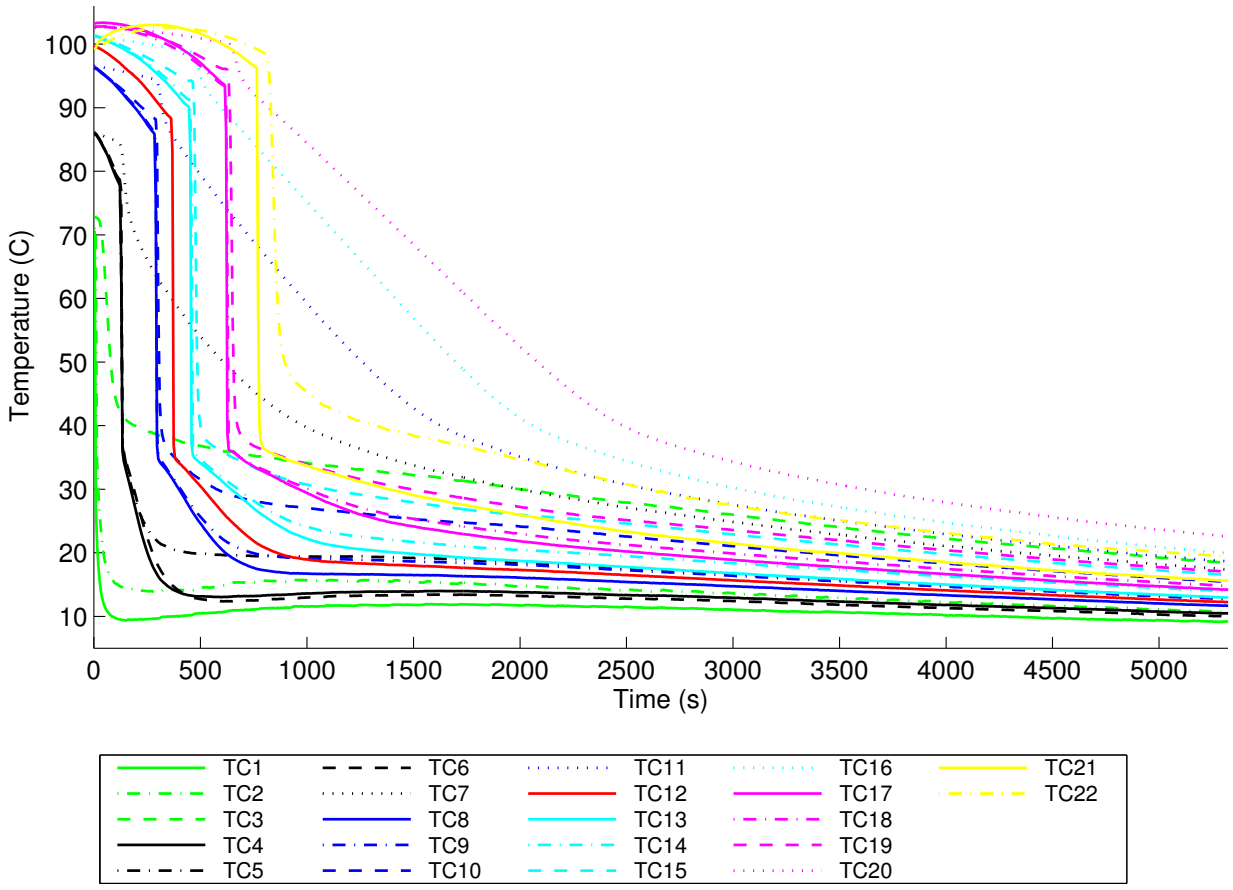

Figure 3.2: Temperature vs time data from twenty-two thermocouples from experimental flow run #1 operated at 200 ml/min flow rate, 82 bar back pressure, and an initial vessel temperature of 100 °C

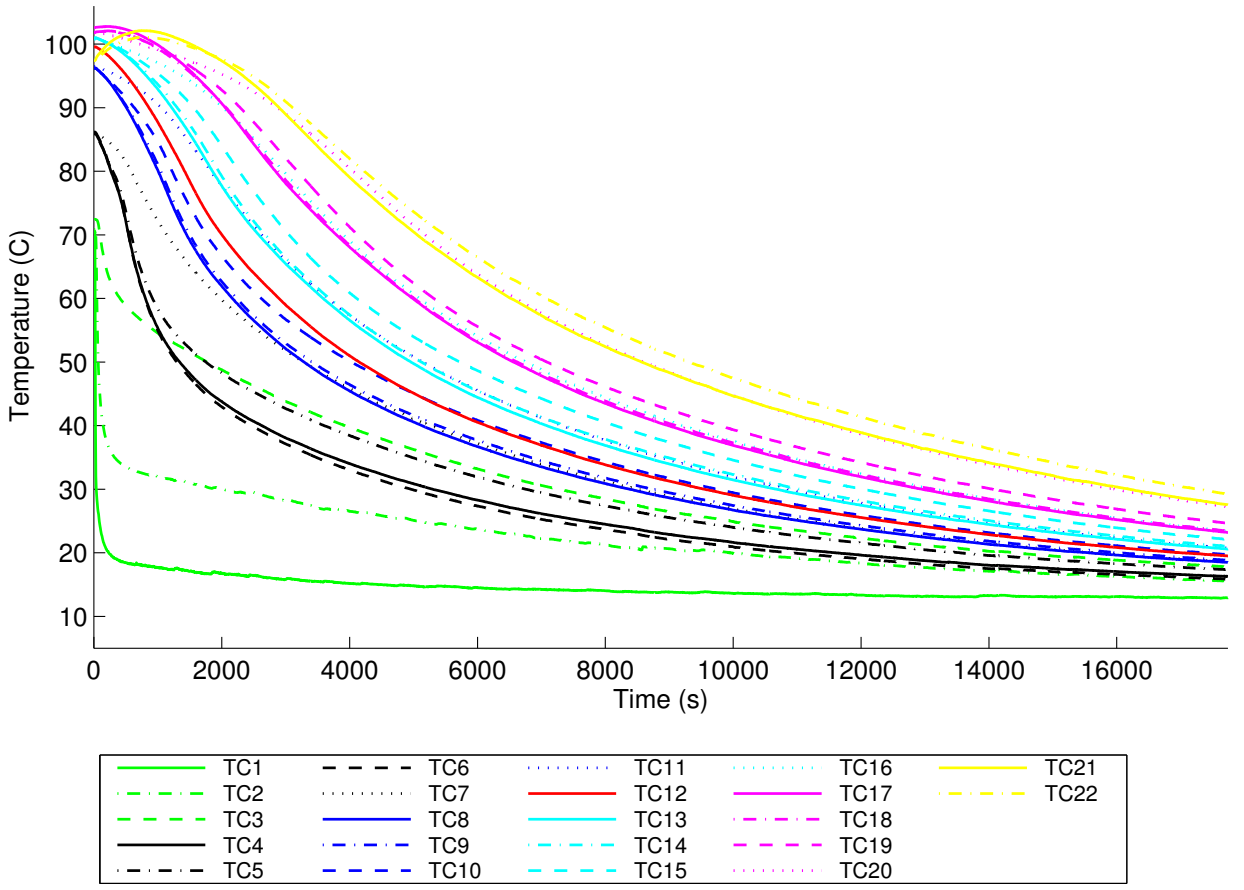

Figure 3.3: Temperature vs time data from twenty-two thermocouples from experimental flow run #2 operated at 50 ml/min flow rate, 147 bar back pressure, and an initial vessel temperature of 100 °C

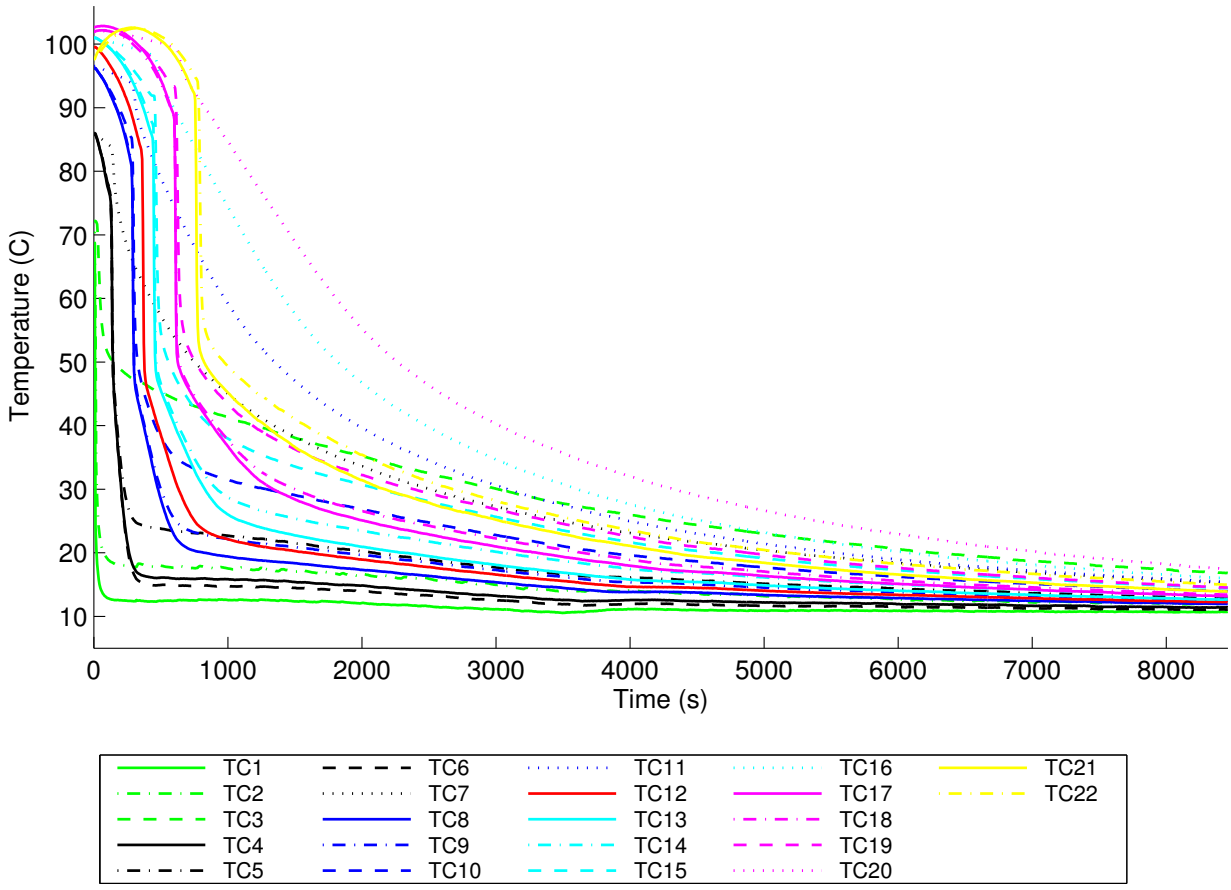

Figure 3.4: Temperature vs time data from twenty-two thermocouples from experimental flow run #3 operated at 200 ml/min flow rate, 108 bar back pressure, and an initial vessel temperature of 100 °C

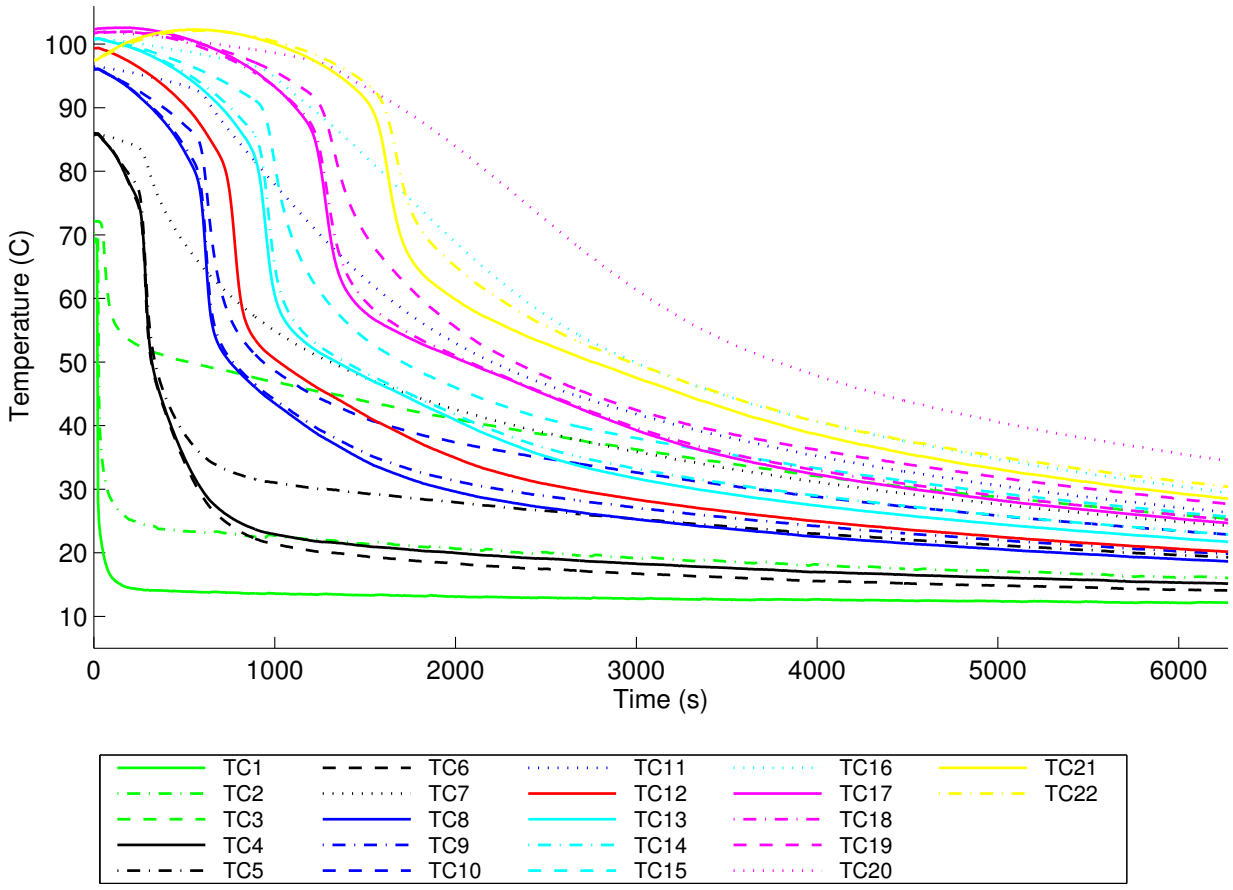

Figure 3.5: Temperature vs time data from twenty-two thermocouples from experimental flow run #4 operated at 100 ml/min flow rate, 108 bar back pressure, and an initial vessel temperature of 100 °C

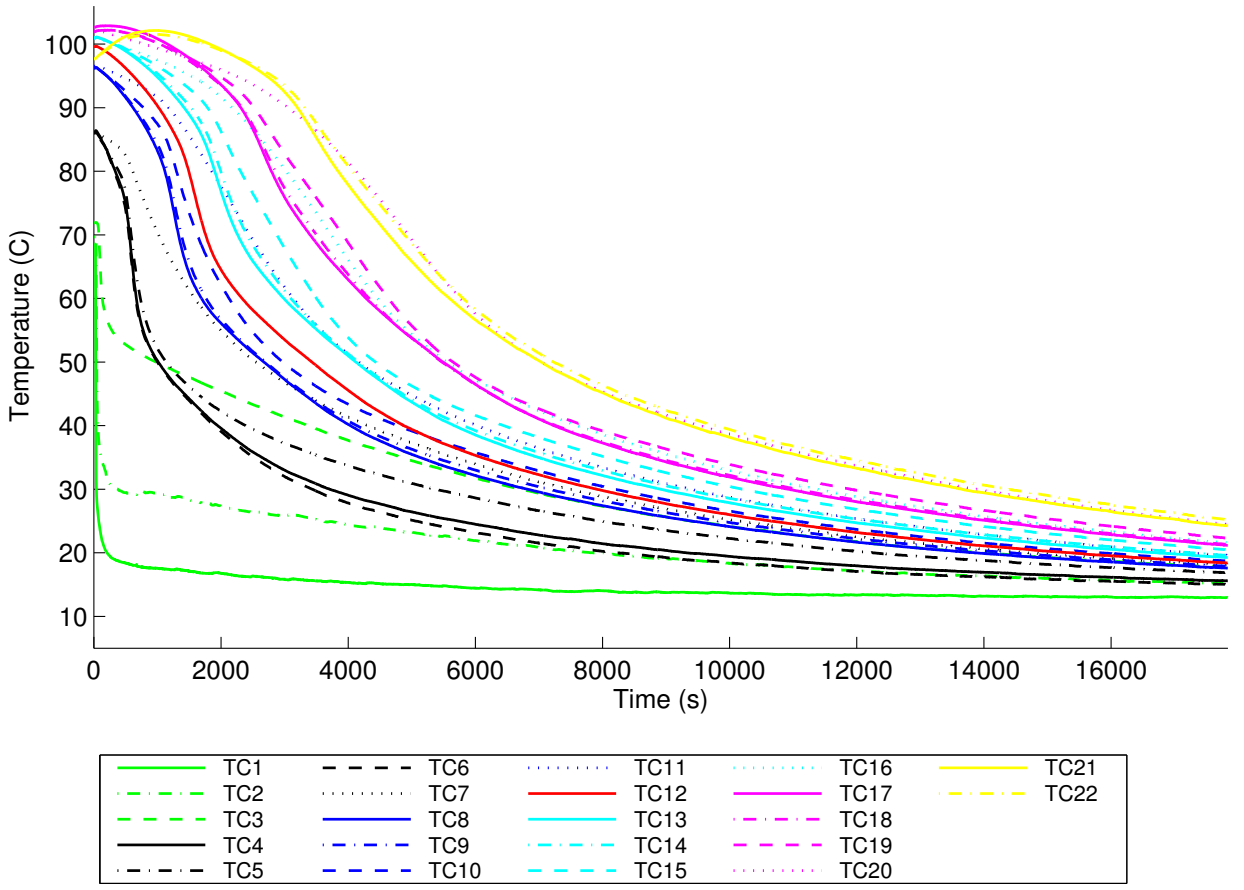

Figure 3.6: Temperature vs time data from twenty-two thermocouples from experimental flow run #5 operated at 50 ml/min flow rate, 108 bar back pressure, and an initial vessel temperature of 100 °C

3.3 Modeling

Modeling Tools

A 2D axisymmetric model of the system was developed in TOUGH2, a numerical simulator for non-isothermal flows of multi-component, multiphase fluids in one, two, and three-dimensional porous and fractured media, and the ECO2N property module which is capable of modeling mixtures of water, NaCl, and CO_2. Version 2.1 of TOUGH2 and version 2.0 of ECO2N was used with the included optional TCSUB code which implements effective thermal conductivity updating as a function of CO_2 thermal conductivity, rock thermal conductivity, and a pore shape parameter (Zimmerman 1989; Pan et al. 2015). During simulations, the standard TOUGH2/ECO2N code will vary the thermal conductivity of grid blocks based only on the degree of saturation by calculating a value based on the thermal

conductivity of the dry and fully saturated block. Without TCSUB enabled, ECO2N does not update the effective thermal conductivity of CO_2 saturated grid blocks despite the fact that the thermal conductivity of CO_2 can vary greatly as a function of pressure and temperature (Chapter 1). The functionality of TCSUB is enabled and disabled by changing the value of the IE(10) parameter in the SELEC block of the input file. An IE(10) value equal to zero will use the default TOUGH2 thermal conductivity handling, and an IE(10) value equal to 2 makes use of the new updating scheme based on effective medium theory (Zimmerman 1989).

TOUGH2 with the ECO2N module was compiled on 64-bit intel Core i3 and Core 2 Duo processors running Ubuntu 14.04 and Mac OS X 10.10 respectively using the GNU fortran compiler gfortran (4.8.2 on Ubuntu and 4.9.2 on the Macintosh). The Mac system was used primarily for model development with coarse meshes while the more computationally robust Ubuntu system was used for finer resolution simulations. The data from the TOUGH2 simulation output file was extracted using the EXT program, the source code of which is freely distributed on the TOUGH2 website. The processed data files were then read into Matlab for analysis and visualization.

A suite of custom Matlab scripts were created that would sequentially generate the model mesh, initialize the model input files based upon the experimental data, initiate the TOUGH2 simulation, process the output file through EXT, import the results into Matlab and analyze and plot the results compared to experimental data. The Matlab mesh generation function is capable of producing a mesh of the appropriate dimensions with user selectable resolution. Besides the back pressure and mass flow rate, the TOUGH2 simulation is initialized with an initial temperature distribution that is derived from the experimental temperature data.

Mesh Design

The model mesh geometry is based upon measurements of the experimental vessel with the exterior surface of the vessel taken as the system boundary (Figure 3.7). The mesh is 2D axisymmetric described on the X-Z plane and revolved around the Z axis creating a series of stacked and nested annuli with the appropriate 3D volumes and surface areas. The mesh blocks were assigned to one of seven different domains: the inlet block, outlet block, passage through the end caps, stainless steel vessel body and end caps, carbon steel vessel nuts, packed sand sample, and sand in contact with the vessel walls. To model the nylon tubing that lines the injection port, the distance between cell center and the interface was increased to slow down the rate of conductive heat transfer from the steel.

Due to the small diameter of the thermocouples and the high temperature gradients present in the vessel during experimental operation, the mesh resolution has an effect on the how the model results are interpreted and matched to the experimental data. TOUGH2 calculates a temperature value for the grid block as a whole, and in order to have TOUGH2 calculate a value that corresponds exactly to a thermocouple measurement the grid blocks would have to have a similar size scale as the thermocouple diameter (0.79 mm), which would be computationally intensive and impractical. Interpolation was employed in order to

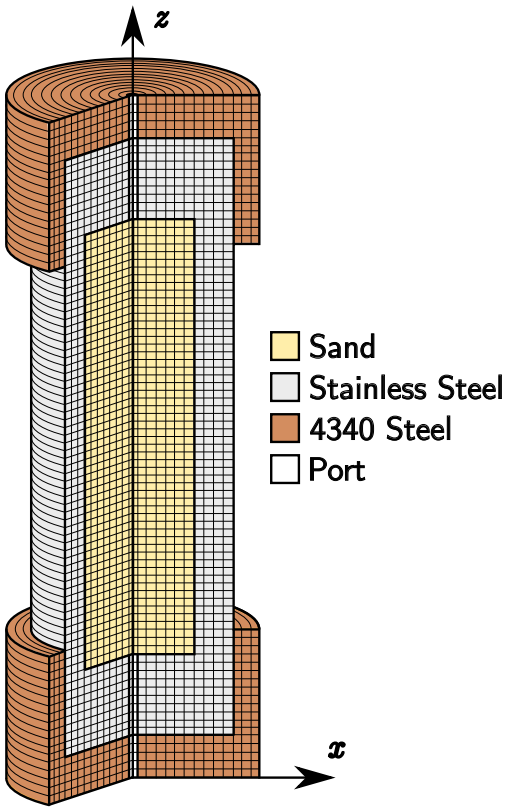

Figure 3.7: Partially revolved model mesh, with colors indicating material type. Not to scale and not representative of final mesh resolution.

approximate the modeled temperature values at thermocouple locations when a larger than thermocouple diameter grid block size is used, the results of which vary depending on the temperature gradient and the mesh resolution especially near boundaries. To explore the sensitivity of the results to grid block size, simulations were run with various mesh resolution. Ultimately a mesh resolution was chosen of approximately 4 mm in the z direction and 8 mm in the x direction.

Domain Properties

The majority of the domain properties such as density, specific heat, and thermal conductivity, were based on standard reference values (Avallone, Baumeister, and Sadegh 2006). The sample porosity was estimated using the measured bulk volume, the mass of packed sand, and the density of quartz. The permeability of the sand was estimated by flowing water at multiple volumetric rates and using the TOUGH2 model to match the measured pressure drop across the sample. To impose a constant temperature on the injection fluid, the injection cell domain was given a very large density and specific heat, and was initialized with the desired injection temperature. To test the the possible effects of greater porosity where the

sand grains meet the vessel wall, a layer of thin grid blocks was placed at the interface and given the same properties as the sand pack but with twice the permeability and porosity. The addition of the sand-wall interface domain had little effect on the simulation results and was ultimately assigned the same properties as the sand pack. The ports passing through the end caps were given a large porosity and permeability to enable free flow, and a thermal conductivity and specific heat that was an estimated average of the CO_2 and a thin layer of steel.

Rock Domain	ρ (kg/m^3)	α (W/(m °C))	C_p(J/(kg °C))	ϕ	Permeability (m^2)
304 Stainless Steel	7500	16.3	500	0	0
4340 Steel	4850	16.3	500	0	0
Quartz Sand	2600	8	830	0.43	3×10^{-10}
Ports	100	5.1×10^{-2}	100	0.99	1×10^{-9}

Table 3.3: Physical properties of model rock domains: Density, Thermal Conductivity, and Specific Heat. (Avallone, Baumeister, and Sadegh 2006)

Boundary Conditions

Three boundary conditions were included in the model, a constant pressure condition at the outlet, a mass flux at the inlet, and heat loss to the lab environment at the vessel exterior. The inlet cell was set as a generation cell with the type set to single phase CO_2 at either a constant mass flow, or a flow rate that varied over time, based on the measured experimental conditions. The outlet cell behavior takes advantage of a TOUGH2 computational shortcut in which the cell is marked as "inactive" and is not included in any of the mass or energy balance equations to ensure that the state does not change from the initial values. The heat loss at the exterior was handled using another TOUGH2 feature in which a semi-analytical function is used to model heat loss to confining geological formations. The approximation of heat loss from the vessel through insulation to relatively well mixed lab air as heat loss to confining geological beds is flawed, but was used for the sake of simplicity to test the sensitivity of the model to any heat loss at the exterior. Heat loss tests were performed by maintaining the temperature of the vessel using the heater tape while measuring the heater tape output. Our estimates show that heat loss during an experiment is approximately 15 to 20 W which is significantly less than the heat loss rate due to CO_2 flow. It was found that including heat loss at the boundary did not significantly improve the fit of the model to measured data.

Model Calibration

Model calibration is required when uncertainty is present in the physical parameters that describe the system being modeled. By carefully varying the uncertain parameters within

a reasonable range, a well designed conceptual model will allow the modeler to refine the parameter estimates and increase the accuracy of the model response. A well designed conceptual model will also enable the modeler to gauge the relative sensitivity of the system to the input parameters. The physical parameters associated with field scale hydrogeological systems often carry significant uncertainty due to the difficulty in characterizing subsurface conditions and the inherent heterogeneity present in natural systems. Laboratory systems usually carry less uncertainty due to the ease of making direct measurements, and the ability to manufacture samples that are essentially homogeneous. Many of the parameters that were used to model the laboratory system were measured directly with relatively high precision, while others parameters were based on reference values which carry their own uncertainty due to manufacturing differences and conflicting published values.

Two parameter estimates used in our system had significant uncertainty, and significant impact to the system response: the permeability of the sand pack, and the effective thermal conductivity of the saturated sand. To estimate the permeability of the sand pack, a series of isothermal single phase flow experiments were performed using water. Water was injected into the sample at varying volumetric flow rates while the pressure drop across the sample was recorded. Water was used instead of CO_2 since the important physical properties of water do not vary significantly in response to pressure and temperature changes. Modeling tools used to model water flow are much more mature and well tested when compared to CO_2 modeling methods. The viscosity of water does change significantly due to temperature, but the relationship is well understood and is easily accounted for. After the water flow measurements were made, the experiments were modeled in TOUGH2 and the permeability value was altered until the model pressure response matched the experimental values across all operating conditions.

The choice of the thermal conductivity input parameters for the model is dependent on the thermal conductivity handling method chosen in the model input file using the IE(10) parameter which enables the TCSUB option. The standard TOUGH2/ECO2N code only changes the thermal conductivity of the grid block based on fluid saturation. The experiments we conducted were under fully saturated conditions at all times so the chosen saturated thermal conductivity value was used throughout the simulation. The modeler must choose a single pressure and temperature at which to make their estimate for thermal conductivity out of the range of pressures and temperatures which occur over time and space during a single experiment. This choice is problematic due to the fact that any estimate will only be valid for limited locations and times within the sample. Furthermore, the value will have to be estimated and calibrated separately for each experimental run based on the unique operating parameters, making the model less deterministic.

Due to the characteristics of the prepared core sample, estimates of effective thermal conductivity made use of a well tested (Woodside and Messmer 1961) model based on an unconsolidated packed bed of uniformly sized spheres (Kunii and Smith 1960). Estimated effective thermal conductivity is a function of the sample porosity and reference values for the thermal conductivity of CO_2 and quartz (Equation 1.5). The minimum and maximum estimated effective thermal conductivity of the saturated medium was calculated for each

experimental run to bound the thermal conductivity input range used for calibration. The calculated values ranged from approximately 0.2 to 1 W/(m K) with the lower value associated with cold injection CO_2 and the higher value with the hot CO_2 present at the initial conditions.

When the new TCSUB code is enabled, the model inputs are the thermal conductivity of the dry rock and a parameter (α) which relates to the shape of the pore space. By basing the thermal conductivity on physical parameters, the model becomes more deterministic and should produce accurate results for all operating conditions. Three limiting shapes have been identified that describe the pore spaces as flat discs ($\alpha = 0$), spherical ($\alpha = 1$), and needle-like pores ($\alpha > 1$) (Zimmerman 1989). For the initial choice we used an α value equal to one, and a reference value for quartz grains situated in random orientations (Woodside and Messmer 1961), this value generated simulation results with a good initial fit to experimental data and allowed us to study the sensitivity of our model to other parameters such as heat loss, the effect of higher porosity at the vessel wall, and mesh resolution.

During calibration it was found that the model temperature output consistently mismatched the experimental data near the end caps of the vessel, this is most likely due to the radial flow that occurs near the end caps which results in very high pore velocities near the injection and outlet ports. The high pore velocities around the inlet and outlet are well outside of the Darcy flow regime and the theoretical capabilities of the TOUGH2 model.

The model also consistently under-predicted the temperature front arrival time at the lower elevations in the sample, this was more apparent at the higher pore velocities present in the higher flow rate experiments indicating this may be due to the upstream prediction errors at the injection end cap propagating up the sample column. When comparing the misfit between simulations, the temperature data at the bottom two thermocouple elevations (numbers 1 through 7) and the highest thermocouples located near the outlet end cap (numbers 21 and 22) were disregarded.

Initial calibration evaluation was graphically based, the simulation results and the experimental results were plotted on the same graph and a subjective determination of fit was made. To further differentiate results a quantitative approach was applied using the weighted mean square error summed over all experiments as a measure of model misfit

$$\Phi = \frac{1}{5}\sum_{j=1}^{5}\frac{1}{k_j}\sum_{t=1}^{k_j}\frac{1}{13}\sum_{i=8}^{20}\frac{\left(d_{ij}(t) - s_{ij}(t)\right)^2}{\sigma^2}, \tag{3.6}$$

where $s_{ij}(t)$ is the simulation results at thermocouple number i at time t from experiment number j, k is the number of simulation time steps, $d_{ij}(t)$ is the recorded experimental data, and σ is the standard deviation of the measurement. To estimate the standard deviation of measurements taking into account error associated with thermocouple placement, assumptions of perfect radial symmetry, and thermocouple measurements themselves, the recorded temperatures of the two thermocouples which had the same elevation and radial location were compared. To estimate the standard deviation it assumed that the mirrored thermo-

couple was an unbiased estimator with respect to thermocouple 15 such that the variance can be determined by the mean squared error

$$\sigma^2 = \frac{1}{n}\sum_{t=1}^{n}\left(tc_{15}(t) - tc_m(t)\right)^2, \tag{3.7}$$

where tc_m is the temperature data recorded by the thermocouple that mirrors tc_{15}.

The misfit values for some different thermal conductivity choices are shown in Table 3.4.

Thermal Conductivity Parameter	Misfit
TCSUB Enabled	
$\alpha = 0.03$	8.26
$\alpha = 0.04$	7.08
$\alpha = 0.05$	6.76
$\alpha = 0.07$	6.56
$\alpha = 0.08$	6.34
$\alpha = 0.1$	6.49
$\alpha = 0.11$	6.73
$\alpha = 0.12$	7.04
$\alpha = 0.5$	9.31
$\alpha = 0.7$	9.43
$\alpha = 1$	9.60
TCSUB Disabled	
$\lambda_{eff} = 0.5$	37.31
$\lambda_{eff} = 1$	16.42
$\lambda_{eff} = 2$	7.78
$\lambda_{eff} = 2.5$	7.25
$\lambda_{eff} = 3$	7.11
$\lambda_{eff} = 3.5$	7.87

Table 3.4: Misfit value for various thermal conductivity parameter choices. For models using the TCSUB code the chosen shape parameter α is given, for models run with TCSUB disabled the chosen effective thermal conductivity (λ_{eff}) is given in $\mathrm{W/(m\,K)}$. Misfit, the weighted mean square error, calculated for thermocouples eight through twenty, for all five experiments.

The lowest misfit value was achieved with a α value of 0.08, while the lowest misfit for a single, constant effective thermal conductivity was $3\,\mathrm{W/(m\,K)}$ which is out of the range of expected values. Without the TCSUB code enabled, it would have been difficult to calibrate the model using realistic effective thermal conductivity values using this calibration method.

Modeling Results

Using the TCSUB option ($\alpha = .08$), the calibrated model simulation results for the central thermocouples (radial location = 0) are shown in Figure 3.8 with diamond markers, along with the experimental results shown without markers.

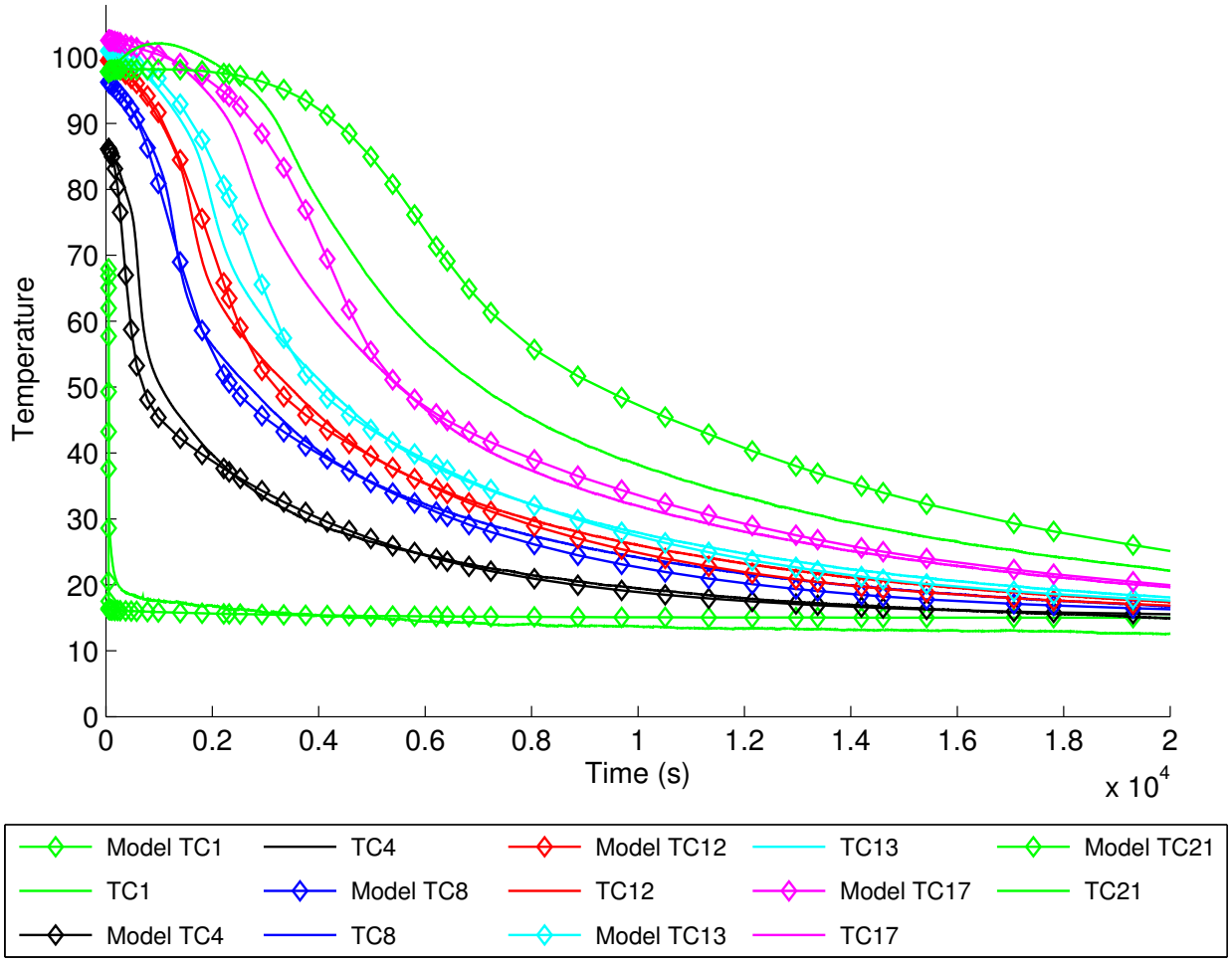

Figure 3.8: Simulations results ($\alpha = 0.08$) compared to data from experiment #5 operated at 50 ml/min flow rate, 108 bar back pressure, and an initial vessel temperature of 100 °C

A good overall fit could be achieved for individual experiments using a carefully chosen and often unrealistic effective thermal conductivity value that was outside of the range supported by theory and research findings. Using reasonable values for λ_{eff} resulted in an overall poor match for all experiments. Figure 3.9 shows the same experiment as in Figure 3.8 in order to compare the effect of choosing a reasonable single effective thermal conductivity (λ_{eff} =1 W/(m K)) as opposed to allowing the TCSUB code to repeatedly estimate the value based on pore shape and fluid state for each time step. A $\lambda_{eff} = 1\,\mathrm{W/(m\,K)}$ is on the high

end of the estimates based on the unconsolidated sand model, and the best fit with TCSUB disabled was with a $\lambda_{eff} = 3\,\mathrm{W/(m\,K)}$.

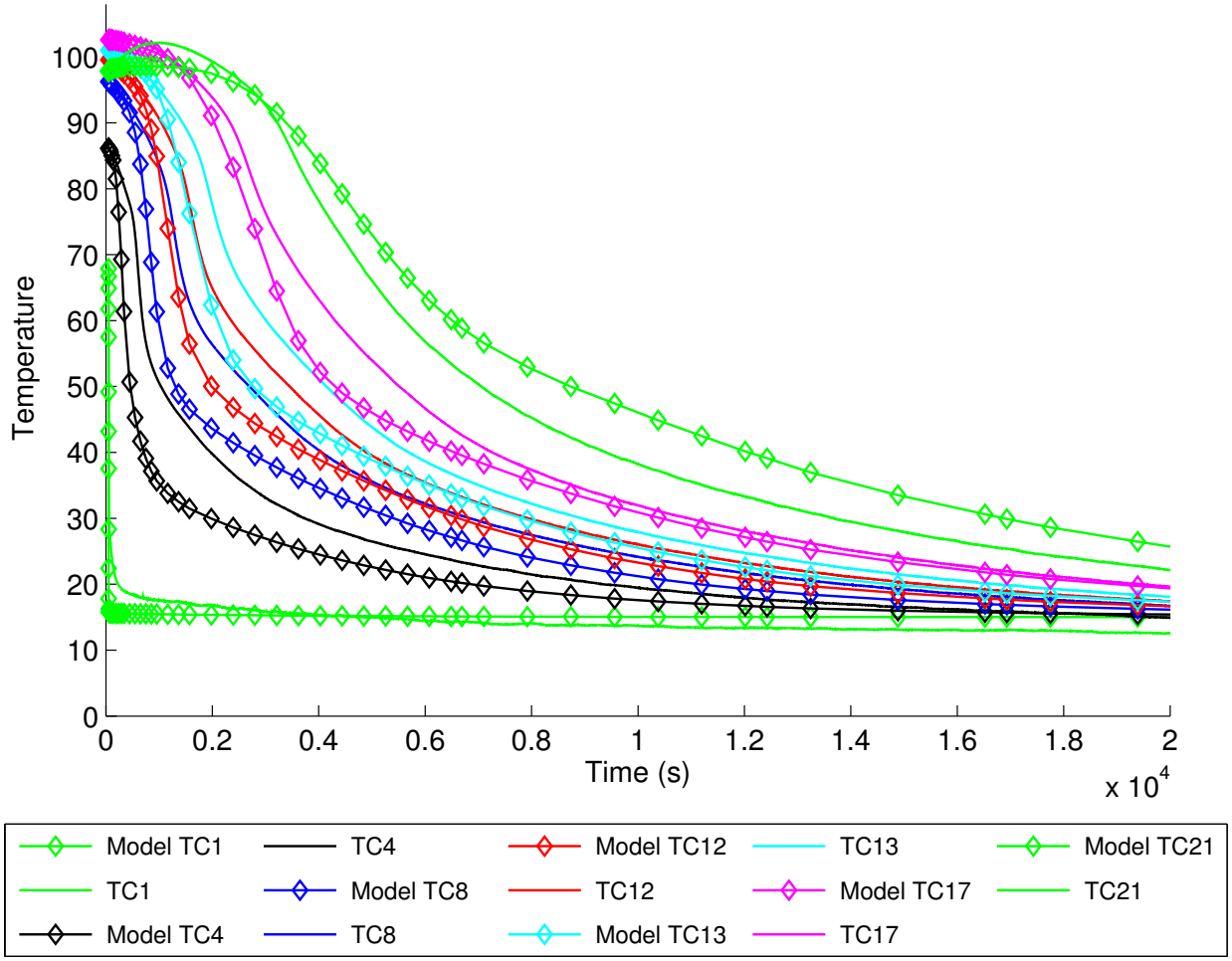

Figure 3.9: Simulations results with TCSUB disabled ($\lambda_{eff} = 1$) compared to data from experiment #5 operated at 50 ml/min flow rate, 108 bar back pressure, and an initial vessel temperature of 100 °C

The general temperature trends and front arrival time predictions produced by the simulation are relatively good at locations which are not in contact with the end caps, but the shapes of the curves do not consistently match well with the experimental data. It was possible to get a better curve shape match for a particular experiment with carefully selected α values or even by selecting a single λ_{eff} value, but no one set of thermal conductivity parameters provided a good curve shape match for all experiments. For example, when simulating experiment number 3, an α of 0.03 provided a much better curve shape fit than the optimal choice of an α of 0.08 as shown in Figure 3.10. When the same parameters are compared for simulations of experiment number 5, it can be seen that α of 0.08 provides a

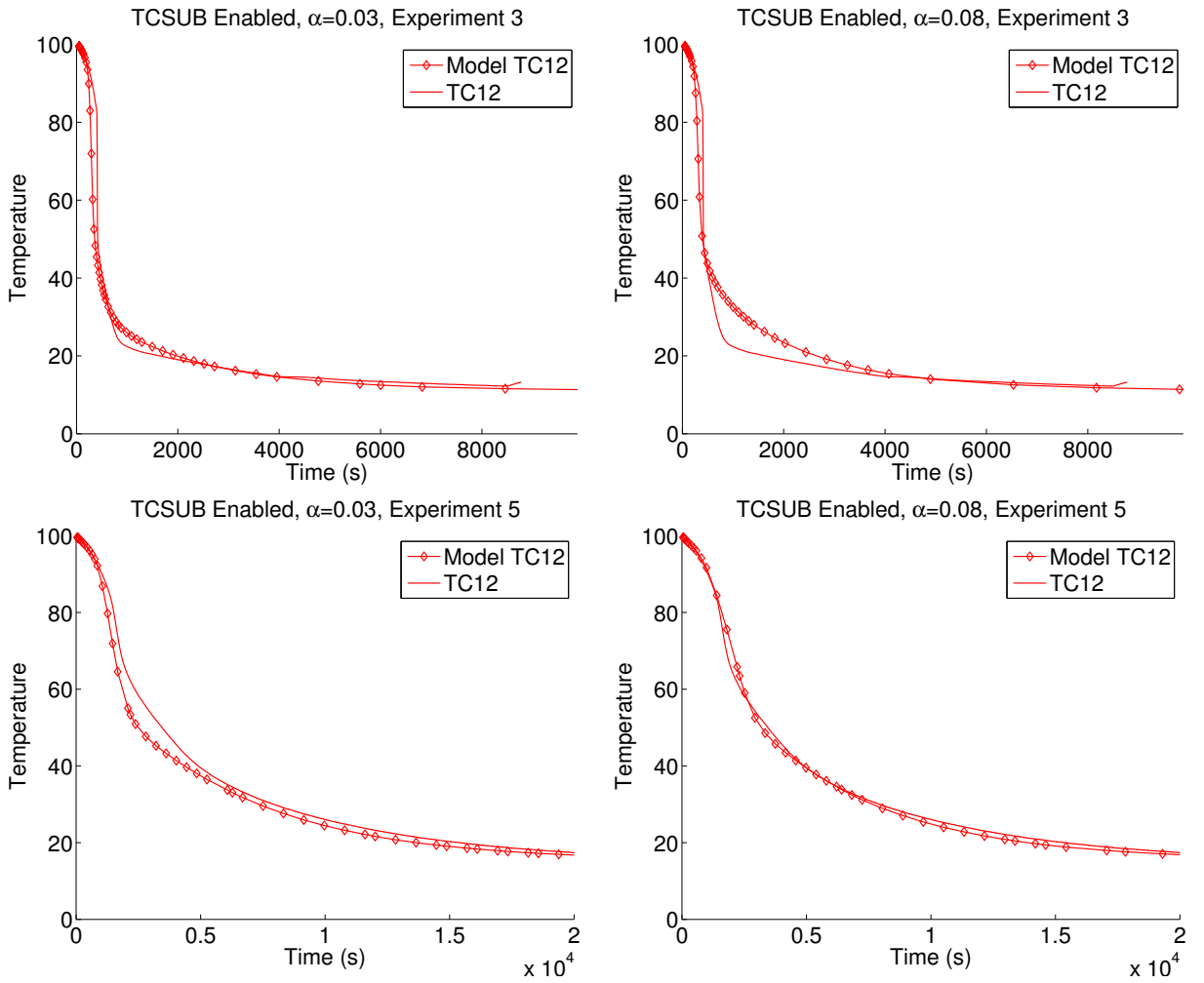

Figure 3.10: Effect of thermal conductivity pore shape parameter on curve shape for experiments # 3 & 5 using an α of 0.03 and 0.08.

better fit for the curve shape. In order to better illustrate the effect of parameter choice on model response, only the most central thermocouple value is shown in Figure 3.10, as it is farthest from all described model boundaries and most dependent on the physical processes described by the model.

The use of the TCSUB code allowed for relatively good fits with a wide range of α choices (Table 3.4), and allowed for much easier model calibration. This indicates that the theoretical basis of the TCSUB code is more accurate than the assumption of constant thermal conductivity of the CO_2 saturated rock. In the original attempts at modeling experiments without TCSUB (Chapter 1), it was difficult to choose a reasonable λ_{eff} that could be used to identify and correct other deficiencies in the model. While TCSUB produced significantly better results, the differences weren't dramatic when compared to results with

TCSUB disabled. This is likely due to the fact that the experiments were not designed to test this specific aspect of the code. The experiments were designed to operate in an advective dominated heat transfer regime, as opposed to a conductively dominated system. In the experimental system, changes in thermal conductivity of the CO_2 are primarily driven by changes in temperature, which is quite drastic in the experiments as can be seen by the steep temperature fronts. Once the initial temperature front passes and the the highly conductive cold CO_2 has displaced the less conductive hot CO_2, there is no longer a large temperature differential present in the region to drive conductive heat transfer. An experiment design with a lower volumetric flow rate and with a constant heat input at the vessel boundary would be more appropriate for exploring the effect of changing thermal conductivity.

3.4 Discussion

The constructed experimental apparatus was capable of producing temperature, pressure, and mass flow measurements of cold CO_2 flow through a heated porous sample within a convection dominated heat transfer regime and within a friction dominated mass transfer regime that is relevant to geothermal energy production applications. Five experiments were conducted under well controlled conditions, and the resulting data was subsequently used for model validation. The results of the experiments and the modeling show that TOUGH2 with the TCSUB option enabled in the ECO2N module is capable of simulating heat transfer in CO_2 saturated porous media with reasonable accuracy with minimal calibration and using reference values for material properties and direct measurements of our system. This is an improvement over the previous version of ECO2N that required the modeler to choose an unreasonable value for the effective thermal conductivity of the CO_2 saturated media for each separate experiment in order to get a reasonable model fit. The new method enabled by the use of TCSUB is more deterministic in nature and more conceptually sound.

The modeling results did not match well with experimental data at locations near the end caps and just downstream of the end caps, most likely due to the converging and diverging radial flow patterns that result in higher pore velocities in the areas. This effect could be minimized if a well insulated space was created at the bottom and top of the vessel in which the fluid flow could spread out or converge with minimal transfer of heat from from the vessel wall or sample. Creating this expansion space would be difficult as it would have to be separated from the sand sample by a permeable and low conductivity barrier. Alternatively, an insert could be created that would alter the cross sectional area of the vessel so it would change gradually from the passage area to the vessel area over some distance.

Since the experimental parameters were chosen to produce convectively dominated heat transfer, the simulation results which made use of the TCSUB code did not produce a significantly better fit to the data than when a carefully selected, but physically unreasonable, constant effective thermal conductivity was used with the TCSUB code disabled. To further test the performance of the TCSUB functionality new experiments should be performed within a conductively dominated heat transfer regime with the possible inclusion of a heat

input at the vessel exterior that would allow a strong and sustained radially oriented thermal gradient to develop.

3.5 Conclusion

This work demonstrates the first use of the TCSUB functionality for modeling CO_2-based heat transfer behavior based on experimental measurements outside of the original developer. Though the experimental results were not optimized to highlight the effectiveness of the new thermal conductivity updating functionality, the modeling results produced less misfit across all experimental runs than when a single reasonable constant effective thermal conductivity was used. While the TCSUB code does require the modeler to choose a pore shape parameter which is an unmeasurable quantity, the sensitivity of the system to the choice was not as great as the sensitivity to the choice of effective thermal conductivity when TCSUB is disabled, allowing more rapid and reasonable model calibration.

TOUGH2 compiled with the ECO2N V2.0 property module is capable of modeling the constructed system with a reasonable accuracy away from the end caps, but more work remains in the process of model validation. The software package iTOUGH, also developed and distributed by Lawrence Berkeley Labs, is capable of performing rigorous statistically-based inverse modeling, model calibration, and sensitivity analysis on TOUGH2 models or any software model that makes use of the PEST interface (Finsterle 2000). Other sources of error and uncertainty in the experimental system and in the numerical modeling code should be identified by performing more experiments with a lower Peclet number, and through the use of the iTOUGH package.

Chapter 4

Conclusion

Lab based experiments and numerical simulations were conducted to investigate the heat transfer behavior of CO_2 flowing through porous media operated within heat and mass transfer regimes that are applicable to enhanced geothermal energy production. An experimental apparatus was designed and constructed that featured boundary controls and a geometry that could be readily implemented within a numerical model. The final apparatus was comprised of a heated sand packed pressure vessel held at a set back pressure, through which temperature controlled CO_2 could be injected at prescribed rates. Experimental operating parameters were chosen to ensure the system was operating in a conductively dominated heat transfer regime similar to field scale geothermal projects while staying within a viscosity dominated mass transfer regime implemented in the numerical modeling tools. The physical and chemical properties and behaviors of CO_2 required the identification of tools, techniques and materials in order to provide sufficient integrity and control of the apparatus. A series of experiments were performed with the completed apparatus that measured the temperature within the sample at many locations, the inlet pressure, the outlet pressure, the rate of fluid injection, and the mass flow rate at the outlet.

The experimental temperature data exhibited time history curves that correspond well to the estimated Peclet number with very steep temperature fronts that traveled upwards through the sample associated with high Pe number estimates and gentle gradual temperature fronts that were associated with lower estimated Pe numbers. The experimental data has shown that the heat transfer behavior was tunable based on the choice of vessel back pressure and the selected fluid injection rate. Energy analysis was performed that showed how the performance of the system was affected by the fluid injection rate. The experimental system exhibited large changes in mass as CO_2 accumulated in the vessel during the course of a run, a behavior that has significant implications for CO_2 based geothermal and CO_2 sequestration projects. Test were also conducted that showed that CO_2 injected into water saturated media will form preferential pathways that bypass the majority of the sample displacing little of the original water.

A detailed TOUGH2 model of the system was implemented and experiments were simulated using the ECO2N property module. Initial attempts at calibrating the model to

experimental measurements produced a poor fit in part due to the incorrect assumption of constant effective thermal conductivity (λ_{eff}) of the CO_2 saturated media that was implicit in TOUGH2. After collecting additional data with an updated version of the apparatus, model calibration was attempted again using ECO2N V2.0 that included optional code that implemented effective thermal conductivity updating. Model calibration with TCSUB enabled was more straight forward as the α parameter choice was independent of experimental operating conditions and the model results were less sensitive to variations in α than to λ_{eff} when TCSUB was disabled. The misfit of the calibrated model across all experiments was lower with TCSUB code enabled than the misfit of the model using a reasonable constant effective thermal conductivity value.

This work has demonstrated that the TOUGH2 modeling code along with the ECO2N V2.0 property module is capable of practical simulations of the heat transfer behavior of CO_2 flowing through porous media within mass and heat transfer regimes that are applicable to enhanced geothermal projects. The simulation results at locations away from the vessel end caps were matched experimental results well and provide more confidence in the tool set for modeling CO_2 geothermal projects. Further work should be conducted at higher temperatures and within more conductively dominated heat transfer regimes in order to better test the performance of the new effective thermal conductivity updating and extended temperature capabilities of ECO2N V2.0.

Bibliography

Aquilina, Luc et al. (2004). "Porosity and fluid velocities in the upper continental crust (2 to 4 km) inferred from injection tests at the Soultz-sous-Forêts geothermal site". In: *Geochimica et cosmochimica acta* 68.11, pp. 2405–2415.

Avallone, Eugene A, Theodore Baumeister, and Ali Sadegh (2006). "Marks' Standard Handbook For Mechanical Engineers (Standard Handbook for Mechanical Engineers)". In:

Barsan, Michael E (2010). *NIOSH pocket guide to chemical hazards*. Centers for Disease Control and Prevention.

Brown, Donald W (2000). "A hot dry rock geothermal energy concept utilizing supercritical CO2 instead of water". In: *Proceedings of the twenty-fifth workshop on geothermal reservoir engineering, Stanford University*, pp. 233–238.

Davies, OM, JC Arnold, and S Sulley (1999). "The mechanical properties of elastomers in high-pressure CO2". In: *Journal of materials science* 34.2, pp. 417–422.

Eastman, Alan D, Mark P Muir, and GreenFire Energy (2013). "CO2 EGS and the Utilization of Highly Pressurized CO2 for Purposes Other Than Power Generation". In: *Proceedings of the Thirty-Eighth Workshop on Geothermal Reservoir Engineering Stanford University*.

Finsterle, S (2000). *ITOUGH2 A Users Guide Rev. 2*. Report LBNL-40040. Lawrence Berkeley Lab., CA (United States).

Friedrich, JP, GR List, and AJ Heakin (1982). "Petroleum-free extraction of oil from soybeans with supercritical CO2". In: *Journal of the American Oil Chemists Society* 59.7, pp. 288–292.

Guiochon, Georges and Abhijit Tarafder (2011). "Fundamental challenges and opportunities for preparative supercritical fluid chromatography". In: *Journal of Chromatography A* 1218.8, pp. 1037–1114.

Kazarian, Sergei G et al. (1996). "Specific intermolecular interaction of carbon dioxide with polymers". In: *Journal of the American Chemical Society* 118.7, pp. 1729–1736.

King, S, F Beck, and U Lüttge (2004). "On the mystery of the golden angle in phyllotaxis". In: *Plant, Cell & Environment* 27.6, pp. 685–695.

Kunii, Daizo and JM Smith (1960). "Heat transfer characteristics of porous rocks". In: *AIChE Journal* 6.1, pp. 71–78.

Lemmon, EW, MO McLinden, and DG Friend (2005). *NIST Chemistry WebBook, NIST Standard Reference Database Number 69*. Ed. by EW Lemmon, MO McLinden, and

DG Friend. Gaithersburg MD, 20899: National Institute of Standards and Technology. Chap. Thermophysical properties of fluid systems. URL: `http://webbook.nist.gov`.

Liao, SM and TS Zhao (2002). "Measurements of heat transfer coefficients from supercritical carbon dioxide flowing in horizontal mini/micro channels". In: *Journal of Heat Transfer* 124.3, pp. 413–420.

Majer, Ernest L et al. (2007). "Induced seismicity associated with enhanced geothermal systems". In: *Geothermics* 36.3, pp. 185–222.

McCune, LK and RH Wilhelm (1949). "Mass and Momentum Transfer in a Solid-Liquid System". In: *Industrial & Engineering Chemistry* 41.6, pp. 1124–1134.

Narasimhan, Arunn and José L Lage (2005). *Variable viscosity forced convection in porous medium channels*. Taylor & Francis, New York.

Pan, Lehua et al. (2015). *ECO2N V2.0: A TOUGH2 Fluid Property Module for Mixtures of Water, NaCl, and CO2*. Report LBNL-6930E. Lawrence Berkeley Lab., CA (United States).

Powell, RW, Cho Yen Ho, and Peter Edward Liley (1966). *Thermal conductivity of selected materials*. Tech. rep. DTIC Document.

Pruess, Karsten (2004). "The TOUGH codesa family of simulation tools for multiphase flow and transport processes in permeable media". In: *Vadose Zone Journal* 3.3, pp. 738–746.

— (2006). "Enhanced geothermal systems (EGS) using CO 2 as working fluida novel approach for generating renewable energy with simultaneous sequestration of carbon". In: *Geothermics* 35.4, pp. 351–367.

— (2007). "Enhanced Geothermal Systems (EGS) comparing water with CO2 as heat transmission fluids". In:

Pruess, Karsten and Nicolas Spycher (2007). "ECO2N–A fluid property module for the TOUGH2 code for studies of CO 2 storage in saline aquifers". In: *Energy Conversion and Management* 48.6, pp. 1761–1767.

Pruess, Karsten et al. (2004). "Code intercomparison builds confidence in numerical simulation models for geologic disposal of CO 2". In: *Energy* 29.9, pp. 1431–1444.

Randolph, Jimmy B and Martin O Saar (2011). "Coupling carbon dioxide sequestration with geothermal energy capture in naturally permeable, porous geologic formations: Implications for CO 2 sequestration". In: *Energy Procedia* 4, pp. 2206–2213.

Rosenbauer, Robert J, James L Bischoff, and Jared M Potter (1993). "A flexible Au-Ir cell with quick assembly for hydrothermal experiments". In: *American Mineralogist* 78.11-12, pp. 1286–1289.

Schremp, FW, GR Roberson, et al. (1975). "Effect of supercritical carbon dioxide (CO2) on construction materials". In: *Society of Petroleum Engineers Journal* 15.3, pp. 227–33.

Tester, Jefferson W et al. (2006). "The future of geothermal energy: Impact of enhanced geothermal systems (EGS) on the United States in the 21st century". In: *Massachusetts Institute of Technology* 209.

Wit, Joeri de and James Wilen (2010). *Economics of Californias Geysers Geothermal Steam Field*. Tech. rep. Department of Agriculture and Resource Economics University of California Davis.

Woodside, W t and JH Messmer (1961). "Thermal conductivity of porous media. I. Unconsolidated sands". In: *Journal of applied physics* 32.9, pp. 1688–1699.

Zeng, Zhengwen and Reid Grigg (2006). "A criterion for non-Darcy flow in porous media". In: *Transport in Porous Media* 63.1, pp. 57–69.

Zimmerman, Robert W (1989). "Thermal conductivity of fluid-saturated rocks". In: *Journal of Petroleum Science and Engineering* 3.3, pp. 219–227.